Lattice NRQCD study of S- and P-wave bottomonium states in a thermal medium with N_{f}=2+1 light flavors

Seyong Kim, Peter Petreczky, and Alexander Rothkopf

Phys. Rev. D **91**, 054511 — Published 25 March 2015

DOI: 10.1103/PhysRevD.91.054511

Lattice NRQCD study of S- and P-wave bottomonium states in a thermal medium with $N_f = 2 + 1$ light flavors

Seyong Kim
Department of Physics, Sejong University, Seoul 143-747, Korea

Peter Petreczky
Physics Department, Brookhaven National Laboratory, Upton, NY 11973, USA

Alexander Rothkopf
Institute for Theoretical Physics, Heidelberg University, Philosophenweg 16, 69120 Heidelberg, Germany

We investigate the properties of S-and P-wave bottomonium states in the vicinity of the deconfinement transition temperature. The light degrees of freedom are represented by dynamical lattice QCD configurations of the HotQCD collaboration with $N_f = 2+1$ flavors. Bottomonium correlators are obtained from bottom quark propagators, computed in Non-Relativistic QCD (NRQCD) under the background of these gauge field configurations. The spectral functions for the ${}^3S_1$ (Υ) and ${}^3P_1$ (χ_{b1}) channel are extracted from the Euclidean time correlators using a novel Bayesian approach in the temperature region 140MeV $\leq T \leq$ 249MeV and the results are contrasted to those from the standard Maximum Entropy Method. We find that the new Bayesian approach is far superior to the Maximum Entropy Method. It enables us to study reliably the presence or absence of the lowest state signal in the spectral function of a certain channel, even under the limitations present in the finite temperature setup. We find that χ_{b1} survives up to $T = 249$MeV, the highest temperature considered in our study and put stringent constraints on the size of the medium modification of Υ and χ_{b1} states.

I. INTRODUCTION

Heavy quarkonium plays an important role in furthering our quantitative understanding of Quantum Chromo Dynamics (QCD) and has been the focus of many experimental and theoretical studies. In particular the large heavy quark mass, relative to the intrinsic scales of its environment, provides a basis for various effective field theory descriptions and allows us to disentangle the short distance perturbative aspects from the non-perturbative long distance effects in QCD [1–3].

The in-medium modification of quarkonium properties, the most dramatic being its melting, has been suggested as a clean signature of Quark-Gluon Plasma (QGP) formation in heavy-ion collisions [4–6]. In our current understanding, the medium screens the interactions between the heavy quark–anti-quark pair (Debye screening) and hence weakens the binding between them. Scattering of medium partons off the gluons, which mediate the interquark binding (Landau damping) [17–19] and absorption of gluons from the medium (singlet-octet transitions) [19] further disturbs the bound state. Ultimately the combination of these effects will prevent the existence of quarkonium states as temperature and/or density increases. Such mechanisms may experimentally manifest themselves as reduced production rates of heavy quarkonium. Early experiments indeed confirmed J/ψ suppression [7] but it was soon discovered that the actual charmonium production in nuclear collision is far more complicated [8] than a simple screening argument suggests.

There are many competing processes that lead to a modification of the measured yields: cold nuclear matter effects, shadowing, gluon saturation and even regeneration of charmonium (instead of suppression) may occur [9]. Thus, careful understanding of each effect is necessary before charmonium suppression, seen in experiments, can be attributed to QGP formation. In this regard, the bottomonium system may turn out to be a more appropriate candidate to investigate the physics of melting. The bottom quark mass is significantly heavier than the charm quark mass and hence the effects of the medium modification are expected to be dominant over e.g. regeneration.

Interestingly, the CMS experiment at LHC discovered a clear pattern of "sequential suppression" among the Υ states: the di-muon distribution around the Υ mass in lead-lead collisions, compared to that in proton-proton collisions, revealed a substantial reduction of $\Upsilon(2S)/\Upsilon(1S)$ and $\Upsilon(3S)/\Upsilon(1S)$ production rates [10, 11].

One way of exploring the in-medium modification of bottomonium from first principles is to use a lattice regularized form of NRQCD [12–14], an effective field theory of QCD. It is formulated using non-relativistic Pauli-spinors, which propagate in the background of otherwise relativistic medium gauge fields, defined on a spacetime lattice. Below the heavy quark mass scale, observables of QCD which are dominated by infra-red physics are well reproduced within this effective description. The non-perturbative character of lattice NRQCD is well suited for the regime where T is only slightly larger than the transition temperature (in which the strong interactions can still be considered "strong" [15, 16]). Being based on an expansion of the QCD action, the effective description can be systematically improved to reproduce more and

more closely relativistic QCD itself.

If one further assumes that the inverse size of the heavy quark bound states is much larger than the binding energy, another effective theory, namely potential NRQCD (pNRQCD) can be constructed. The potentials entering in this Effective Field Theory (EFT) can be related to Wilson loops and in the simplest formulation one encounters a quantum mechanical problem [17–21]. Depending on the relation between inverse size and the temperature of the system, the potentials can be also temperature dependent. However, the scale separation required for utilizing pNRQCD is more difficult to justify and in this sense NRQCD is more robust.

Recent lattice studies of in-medium bottomonium on anisotropic lattices at non-zero temperature concluded that the ground state ($1S$) peak of the Υ spectral function (obtained from the Maximum Entropy Method (MEM) [22, 23]) survives up to $\sim 2T_c$, and the excited state ($2S, 3S$) peaks in this vector channel spectral function disappear gradually as the temperature increases above T_c [24–26]. A study of P-wave bottomonium states, such as χ_{b1}, in lattice NRQCD using the MEM furthermore concluded that the ground state "melts" almost immediately above T_c [24, 26, 27]. It has to be kept in mind however that e.g. the pion mass in these studies remained rather heavy with $M_\pi \simeq 400$ MeV.

In this work, we report on a lattice NRQCD study of bottomonium in 2+1 flavor QCD below and above the chiral transition using HotQCD configurations, generated with Highly Improved Staggered Quark (HISQ) action on isotropic $48^3 \times 12$ lattices [28] (see a preliminary report in [29]). The gauge configurations have been generated for a physical value of the strangle quark mass m_s and light quark masses $m_l = m_s/20$ that in the continuum limit correspond to pion mass of $M_\pi = 161$ MeV, only slightly above the physical pion mass of 140 MeV.

Previous lattice NRQCD studies at non-zero temperature used a fixed lattice scale approach, where the inverse temperature is available only at integer steps. Here we achieve a finer temperature scan by changing the lattice spacing instead. Note that at each coupling an accompanying zero temperature lattice simulation is required to set the absolute energy scale.

An accurate and precise extraction of spectral functions using the standard MEM is difficult, since the number of lattice points in imaginary time direction is typically small. More importantly it is the extent of the imaginary time in physical units that decreases with increasing temperature. The underlying technical reason is that the small number of lattice sites in temporal direction ($N_\tau = 12$) limits the number of basis functions available in the MEM search space, which relies on a singular value decomposition.

Instead, we deploy a new Bayesian method [30, 31] and compare its results with those obtained using conventional Bryan's MEM. Based on the same data, the new method produces in general sharper, i.e. more highly resolved spectral features for both Υ and χ_{b1} and allows better control over most of the systematic errors associated with the spectral function reconstruction. While systematic uncertainties resulting from a small N_τ still prevents us to provide quantitative estimates of the in-medium mass shifts and widths, the higher precision allow us to put stringent upper limits on these effects.

Despite the difference, Υ spectral functions from the improved Bayesian method and those from MEM both show a similar qualitative temperature dependence: the ground state peak of the Υ channel survives up to the highest temperature ($T = 249$MeV we studied. For the P-wave channel, the difference is more substantial. The first peak in the χ_{b1} spectral function obtained from the improved Bayesian method survives to 249MeV but in the result based on the MEM it disappears for $T \gtrsim 211$MeV.

In the first part of section II we briefly review the lattice formulation of NRQCD and specify pertinent technical details underlying the measurements of the bottomonium correlators. The second part contains the basics of the novel Bayesian method, which we deploy in the extraction of the bottomonium spectra. Section III describes the calibration of the NRQCD mass scale carried out on low temperature lattices, while in section IV we present the central results of our study, the spectral properties of in-medium bottomonium at temperatures around the deconfinement transition temperature. We end the main part of the manuscript in section V with concluding remarks. The systematic uncertainties of the spectral reconstructions, as well as dependencies on the NRQCD discretization are investigated and discussed in two separate appendices A and B respectively.

II. NUMERICAL METHODS

A pronounced separation of scales invites the use of effective field theoretical methods for the description of in-medium bottomonium. Indeed, the heavy quark mass $M_b \simeq 4.6$GeV [32] and the intrinsic scale of QCD $\Lambda_{\rm QCD} \sim 200$MeV, as well as the typical momentum exchange within a possible bound state lie widely apart. The presence of a thermal medium introduces an additional scale T, which however also lies well below the bottom quark rest mass in current heavy-ion collision experiments.

In an EFT, the physics above the energy of interest is *integrated out* [2], which requires one to determine the relevant degrees of freedom within the hierarchy of scales present in the system. To avoid the intricacies of relative scale ordering in the presence of finite temperature, we will deploy here a lattice regularized version of NRQCD, where only the hard scale M_b, i.e. the bottomonium rest mass is integrated out. The heavy quarks appear as non-relativistic Pauli spinors, which propagate under the background of the light medium degrees of freedom (in our case gluons, up, down and strange quarks), which themselves are in thermal equilibrium.

The non-perturbative character of the EFT description is of the essence, since close to the transition temperature the QGP still remains strongly correlated and temperature effects on the binding dynamics ($\sim M_b v$), which are our main interest, will not be perturbative.

Lattice NRQCD

In order to investigate the properties of bottomonium in a thermal medium, we compute the correlators of heavy quarkonium using a lattice discretization of the $\mathcal{O}(v^4)$ NRQCD Lagrangian [13, 35, 36] for bottom quarks,

$$\mathcal{L} = \mathcal{L}_0 + \delta\mathcal{L}, \tag{1}$$

with

$$\mathcal{L}_0 = \psi^\dagger \left(D_\tau - \frac{\mathbf{D}^2}{2M_b}\right)\psi + \chi^\dagger \left(D_\tau + \frac{\mathbf{D}^2}{2M_b}\right)\chi, \tag{2}$$

and

$$\begin{aligned}\delta\mathcal{L} =& -\frac{c_1}{8M_b^3}\left[\psi^\dagger(\mathbf{D}^2)^2\psi - \chi^\dagger(\mathbf{D}^2)^2\chi\right] + c_2\frac{ig}{8M_b^2}\left[\psi^\dagger\left(\mathbf{D}\cdot\mathbf{E} - \mathbf{E}\cdot\mathbf{D}\right)\psi + \chi^\dagger\left(\mathbf{D}\cdot\mathbf{E} - \mathbf{E}\cdot\mathbf{D}\right)\chi\right] \\ & -c_3\frac{g}{8M_b^2}\left[\psi^\dagger\boldsymbol{\sigma}\cdot\left(\mathbf{D}\times\mathbf{E} - \mathbf{E}\times\mathbf{D}\right)\psi + \chi^\dagger\sigma\cdot\left(\mathbf{D}\times\mathbf{E} - \mathbf{E}\times\mathbf{D}\right)\chi\right] - c_4\frac{g}{2M_b}\left[\psi^\dagger\sigma\cdot\mathbf{B}\psi - \chi^\dagger\sigma\cdot\mathbf{B}\chi\right].\end{aligned}$$

Here D_τ and $\mathbf{D}$ are gauge covariant temporal and spatial derivatives, ψ denotes the heavy quark and χ the heavy anti-quark. From the discretized version of Eq. (1), the lattice NRQCD propagator for the bottom quark is computed as an initial value problem

$$\begin{aligned}G(\mathbf{x},\tau_0) =& \boldsymbol{S}(\mathbf{x}),\\ G(\mathbf{x},\tau_1) =& \left(1-\frac{H_0}{2n}\right)^n U_4^\dagger(\mathbf{x},0)\left(1-\frac{H_0}{2n}\right)^n G(\mathbf{x},0),\\ G(\mathbf{x},\tau_i) =& \left(1-\frac{H_0}{2n}\right)^n U_4^\dagger(\mathbf{x},\tau)\left(1-\frac{H_0}{2n}\right)^n \\ & \times(1-\delta H)\,G(\mathbf{x},\tau_{i-1}).\end{aligned} \tag{3}$$

$S(\mathbf{x})$ denotes an appropriate complex valued random point source, diagonal in spin and color, which is used to improve the signal to noise ratio. In the continuum formulation the initial condition for $G(\mathbf{x},\tau)$ corresponds to a delta function, which we approximate on the lattice through averaging multiple correlators, started from random sources on different slices τ_{start} along Euclidean time e.g.

$$S^\Upsilon(\mathbf{x},\tau_{\text{start}}) = \eta(\mathbf{x},\tau_{\text{start}}), \quad \langle\eta^\dagger(\mathbf{x})\eta(\mathbf{x}')\rangle_{\tau_{\text{start}}} = \delta_{\mathbf{x}\mathbf{x}'} \tag{4}$$

The lowest-order Hamiltonian reads

$$H_0 = -\frac{\Delta^{(2)}}{2M_b}, \tag{5}$$

while

$$\begin{aligned}\delta H =& -\frac{(\Delta^{(2)})^2}{8M_b^3} + \frac{ig}{8M_b^2}(\boldsymbol{\Delta}^\pm\cdot\mathbf{E} - \mathbf{E}\cdot\boldsymbol{\Delta}^\pm) \\ & -\frac{g}{8M_b^2}\boldsymbol{\sigma}\cdot(\boldsymbol{\Delta}^\pm\times\mathbf{E} - \mathbf{E}\times\boldsymbol{\Delta}^\pm) \\ & -\frac{g}{2M_b}\boldsymbol{\sigma}\cdot\mathbf{B} + \frac{a^2\Delta^{(4)}}{24M_b} - \frac{a(\Delta^{(2)})^2}{16nM_b^2}.\end{aligned} \tag{6}$$

Here, n denotes a parameter, which controls the effective temporal step size in Euclidean time, when propagating the Green's function on the lattice. Choosing an appropriate value is essential to the stability of the high momentum behavior of the propagator G. We use $n = 2$, in anticipation of the characteristic values of $M_b a_s$, which will arise on the lattices used in this study. We have checked by varying the parameter n up to values of four that the choice $n = 2$ already allows us to capture the bottomonium bound state physics in a robust manner. A detailed description of these tests can be found in Appendix B.

The lattice covariant derivative Δ is defined as

$$\begin{aligned}a\Delta_i^+\psi(\mathbf{x},\tau) &= U_i(\mathbf{x},\tau)\psi(\mathbf{x}+\hat{i}a,\tau) - \psi(\mathbf{x},\tau)\\ a\Delta_i^-\psi(\mathbf{x},\tau) &= \psi(\mathbf{x},\tau) - U_i^\dagger(\mathbf{x}-\hat{i}a,\tau)\psi(\mathbf{x}-\hat{i}a,\tau)\\ \Delta^{(2)} &= \sum_{i=1}^3\Delta_i^+\Delta_i^-,\ \Delta^{(4)} = \sum_{i=1}^3(\Delta_i^+\Delta_i^-)^2,\end{aligned} \tag{7}$$

and the chromo-electric ($\mathbf{E}$) and the magnetic field ($\mathbf{B}$) are defined from clover-leaf plaquettes. The last two terms of Eq. (6) correct for finite lattice spacing errors. Tad pole improvement of the gauge link variable using the fourth root of a single link plaquette [37] (listed in table II) is adopted and c_i in Eq. (3) is set to the tree-level value (= 1). The bottom quark mass is not tuned using the NRQCD dispersion relation. Instead, $M_b a$ for each lattice spacing is set using $M_b = 4.65$ GeV in the computation (listed in table II).

In this work, a partial set of gauge configurations in 2+1 flavor QCD is used, which is based on the Highly Improved Staggered Quark (HISQ) action with physical strange quark mass, m_s and light quark masses $m_l = m_s/20$ corresponding to a pion mass of 161 MeV in the continuum limit. For the calculations at non-zero temperature the lattice size amounts to $48^3 \times 12$. These

configurations were generated for the study of the finite temperature QCD phase transition described in [28]. The chiral transition temperature in the continuum limit was determined to be 154(9) MeV [28]. On $N_\tau = 12$ lattices used in this study, the central value of the transition temperature is slightly larger, $T_c = 159(3)$ MeV, but still is compatible with the above number within errors. In the following discussion we will use the value $T_c = 154$MeV and often quote the temperature in units of T_c. The lattice parameters are given in Table I and Table II. At $T > 0$ we estimate the correlators on 400 gauge configurations, while at $T \simeq 0$ we use 100 configurations at our disposal.

After gauge fixing into Coulomb gauge, we calculate the bottom quark Green function and subsequently determine the bottomonium correlators

$$D(\mathbf{x},\tau) = \sum_{\mathbf{x}_0} \langle O(\mathbf{x},\tau) G(\mathbf{x},\tau) O^\dagger(\mathbf{x}_0,\tau_0) G^\dagger(\mathbf{x},\tau)\rangle_{\rm med}$$

for each channel

$$O(^3S_1;\mathbf{x},\tau) = \sigma_i, \quad O(^3P_1;\mathbf{x},\tau) = \overset{\leftrightarrow}{\Delta}{}^s{}_i \sigma_j - \overset{\leftrightarrow}{\Delta}{}^s{}_j \sigma_i, \quad (8)$$

with $\chi^\dagger \overset{\leftrightarrow}{\Delta}{}^s{}_i \psi = -\left[\frac{1}{4}\left(\Delta_i^+ + \Delta_i^-\right)\chi\right]^\dagger \psi + \chi^\dagger \left[\frac{1}{4}\left(\Delta_i^+ + \Delta_i^-\right)\psi\right]$ as defined (unfortunately with a typo) in [12]. For example, the Υ channel correlator is computed explicitly as

$$\begin{aligned}
\langle (\chi^\dagger{}_a(\sigma_x)_{ab}\psi_b(x'))^\dagger \chi_c^\dagger(\sigma_x)_{cd}\psi_d(x)\rangle &= 2\langle G_{++}(x';x)^\dagger G_{--}(x';x) + G_{+-}(x';x)^\dagger G_{-+}(x';x)\rangle \\
\langle (\chi_a^\dagger(\sigma_y)_{ab}\psi_b(x'))^\dagger \chi_c^\dagger(\sigma_y)_{cd}\psi_d(x)\rangle &= 2\langle G_{++}(x';x)^\dagger G_{--}(x';x) - G_{+-}(x';x)^\dagger G_{-+}(x';x)\rangle \\
\langle (\chi_a^\dagger(\sigma_z)_{ab}\psi_b(x'))^\dagger \chi_c^\dagger(\sigma_z)_{cd}\psi_d(x)\rangle &= \langle G_{++}(x';x)^\dagger G_{++}(x';x) + G_{--}(x';x)^\dagger G_{--}(x';x) \\
&\quad - G_{+-}(x';x)^\dagger G_{+-}(x';x) - G_{-+}(x';x)^\dagger G_{-+}(x';x)\rangle,
\end{aligned} \quad (9)$$

where $+(-)$ denotes the spin-up (spin-down) component and $\langle\cdots\rangle$ refers to the average over the thermal ensemble. Similarly by using $\chi^\dagger \overset{\leftrightarrow}{\Delta}_i \psi \equiv \chi^\dagger \Delta_i \psi - \Delta_i \chi^\dagger \psi$ we have for the χ_{b1} channel

$$\begin{aligned}
&\langle \left[\chi_a^\dagger \left(\overset{\leftrightarrow}{\Delta}_i (\sigma_j)_{ab} - \overset{\leftrightarrow}{\Delta}_j (\sigma_i)_{ab}\right)\psi_b(x')\right]^\dagger \chi_c^\dagger \left(\overset{\leftrightarrow}{\Delta}_i (\sigma_j)_{cd} - \overset{\leftrightarrow}{\Delta}_j (\sigma_i)_{cd}\right)\psi_d(x)\rangle \\
&= \langle \mathrm{tr}\left[G^\dagger(x';x)\sigma_i\Delta_j G_V(x';x,j)\sigma_i\right]\rangle - \langle \mathrm{tr}\left[{G_V}^\dagger(x';x,j)\sigma_i\Delta_j G(x';x)\sigma_i\right]\rangle \\
&+ \langle \mathrm{tr}\left[G^\dagger(x';x)\sigma_j\Delta_i G_V(x';x,i)\sigma_j\right]\rangle - \langle \mathrm{tr}\left[{G_V}^\dagger(x';x,i)\sigma_j\Delta_i G(x';x)\sigma_j\right]\rangle \\
&- \langle \mathrm{tr}\left[G^\dagger(x';x)\sigma_i\Delta_j G_V(x';x,i)\sigma_j\right]\rangle + \langle \mathrm{tr}\left[{G_V}^\dagger(x';x,j)\sigma_i\Delta_i G(x';x)\sigma_j\right]\rangle \\
&- \langle \mathrm{tr}\left[G^\dagger(x';x)\sigma_j\Delta_j G_V(x';x,i)\sigma_i\right]\rangle + \langle \mathrm{tr}\left[{G_V}^\dagger(x';x,j)\sigma_j\Delta_i G(x';x)\sigma_i\right]\rangle
\end{aligned}$$

Computational cost is reduced by using point split sources (along the i-th direction), from which the propagator $G_V(x';x,i)$ is evolved. "tr" refers to a color and spin trace.

Bayesian spectral reconstruction

While our goal is to determine the spectral properties of in-medium bottom quark-antiquark pairs, lattice QCD only provides us with correlation functions in Euclidean time. In the particular case of NRQCD bottomonium correlators $D(\tau)$, the sought after spectral functions $\rho(\omega)$ can be extracted via the inversion of the following integral relation

$$D(\tau) = D(\mathbf{p}=0,\tau) = \sum_{\mathbf{x}} D(\mathbf{x},\tau) = \int_{-2M_q}^{\infty} d\omega\; e^{-\omega\tau}\; \rho(\omega). \quad (10)$$

The exponentially damped integral Kernel $K(\tau,\omega) = \exp[-\omega\tau]$ is temperature independent, which alleviates the "constant contribution" problem [38–40]. Since NRQCD is an effective non-relativistic description of bottomonium physics, it implicitly contains a shift in energies to the two-quark threshold $2M_q$ (up to renormalization).

Obviously the introduction of a spacetime regularization as the basis for lattice QCD simulations only allows us to obtain the correlation function at N_τ discrete steps of Euclidean time. Furthermore the stochastic character of the Monte Carlo algorithm involved in generating the lattice configurations entails that only estimates of finite precision can be calculated for each observable. Hence the inversion of Eq. (10) becomes inherently ill-defined, as we attempt to extract the spectral features of thermal bottomonium along $N_\omega \gg N_\tau$ frequencies from a finite number of noisy data points.

One possibility to give meaning to the inversion is by making use of prior knowledge in addition to the measured data. Bayes theorem

$$P[\rho|D,I] \propto P[D|\rho,I]P[\rho|I] \tag{11}$$

provides the mathematical framework to do so. Here the likelihood probability $P[D|\rho,I] = \exp[-L]$ is given by

$$L[\rho] = \frac{1}{2}\sum_{ij}(D_i - D_i^\rho)C_{ij}(D_j - D_j^\rho) \tag{12}$$

where C_{ij} denotes the covariance matrix of the measured data and

$$D_i^\rho = \sum_{l=1}^{N_\omega} \exp[-\omega_l\tau_i]\ \rho_l\ \Delta\omega_l \tag{13}$$

denotes the Euclidean correlator, which would result from our current choice ρ. We also enforce the additional constraint $L = N_\tau$, since the correct spectral functions leads to an L value of comparable magnitude. If we were to attempt a naive χ^2 fit, i.e. to maximize the likelihood alone, one encounters an infinite number of degenerate solutions that all reproduce the data points D_i within their errors. Taking into account prior knowledge allows us to regularize the χ^2 fit. The particular functional form of the prior probability $P[\rho|I] = \exp[S]$ selects from the degenerate maximum likelihood solutions a single one that represent the most likely spectrum given the measured data and our prior information.

In this study we use a prior functional S, which has recently been proposed, based on the following three conditions: (1) it enforces that the spectrum is positive definite, (2) it guarantees that the choice of units for $\rho(\omega)$ remains irrelevant for the end result, and (3) that the reconstructed spectrum is a smooth function except where data introduces peaked structures

$$S[\rho] = \alpha\sum_l \left(1 - \frac{\rho_l}{m_l} + \log\Big[\frac{\rho_l}{m_l}\Big]\right)\Delta\omega_l. \tag{14}$$

Note that this expression differs from the Shannon-Jaynes entropy used in the Maximum Entropy Method.

The function $m(\omega_l) = m_l$ residing within S is called the default model and by definition corresponds to the correct spectrum in the absence of data. Since we do not assume any additional knowledge beyond positive definiteness and smoothness, we will use a constant $m(\omega) = \text{const.}$ in the following. As we also measure the data point at $\tau = 0$, which encodes the normalization of the spectrum, we adjust the overall magnitude of the default model accordingly. The dependence of the results on different choices of $m(\omega)$ is investigated in Appendix A.

The hyperparameter α, which controls the weighting of the data versus prior information is taken into account in a Bayesian fashion. In the new Bayesian method deployed here, it is integrated out using a flat overall hyperprior.

$$P[\rho|D,I] = P[D|I]\int_0^\infty d\alpha P[\rho|m,\alpha] \tag{15}$$

Hence we do not rely on the usually poor Gaussian approximation entering the α probability estimation of the MEM (for details see ref.[30]).

The Bayesian reconstruction (BR), given the measured data and our prior knowledge, is thus obtained from finding the the most probable solution for the combined likelihood and prior probability

$$\frac{\delta}{\delta\rho}P[\rho|D,I]\bigg|_{\rho=\rho^{\rm BR}} = 0 \tag{16}$$

In contrast to the standard MEM, we do not restrict the search space a priori but allow the full N_ω degrees of freedom to vary. This not only allows us to resolve spectral peaks with a much smaller width but also removes the strong dependence of the reconstructed peaks on the choice of the starting point of the discretized frequency interval $\omega_{\rm min}$ as shown in Appendix A.

A crucial qualitative difference to the MEM exists in that our prior functional does not possess the flat directions inherent in the Shannon-Jaynes entropy deployed there. This leads to the optimizer algorithm actually converging to a unique extremum up to any desired tolerance. Thus we do not arbitrarily stop the minimizer at a predefined step size but require convergence to machine precision.

To estimate the statistical uncertainty in our results, we perform Jackknife analyses for each spectrum, by repeating the reconstruction procedure and excluding successive blocks of 10 ($T \simeq 0$) or 40 ($T > 0$) configurations from the averaging of the underlying correlators. The variation between each of these results is then used to estimate a Jackknife error-bar which we attach to all quantities plotted in the following section. As is known from prior work with the MEM, the reconstruction, especially of the width of peak structures depends on the amount of available data points as well as the signal to noise ratio. The uncertainty related to these two factors is explicitly assessed in Appendix A.

Once a spectral reconstruction is performed, we need to interpret the outcome in terms of bottomonium physics. On the one hand we need to ascertain whether peaked structures arising in the Bayesian result are actually encoded in the supplied data points and whether

such peaks are indeed an indication of a bound state available to the heavy quark anti-quark pair. The former question is related to the limited amount of data points available along the temporal axis in this study. Indeed even if we discretize the frequency domain between $-2M_q < \omega_{\min} < \omega_{\max} < \infty$ with a large number of $N_\omega \gg N_\tau$ steps of length $\Delta\omega_l$, we will encounter finite resolution artifacts, as is known from the closely related Inverse-Fourier transform. If the spectrum contains a region in which it essentially vanishes before abruptly changing into either peaked structures or at high temperatures into a continuum, any reconstruction based on a finite number of data points will contain some kind of numerical ringing usually referred to as the Gibbs phenomenon. The intensity of these artifacts is furthermore related to the choice of default model, which if incompatible to the encoded spectral structures will exacerbate ringing. In the following we intentionally use the most neutral, i.e. a flat default model and hence need to prepare for the encounter with wiggly structures in the numerical extraction of spectral functions that do not have a physical counterpart encoded in the data.

In addition, we need to understand whether a peak encoded in the data can actually be attributed to the strong interactions binding together bottom quarks into a bound state. Both aspects are addressed in this study through a comparison of the fully interacting spectra to those based on non-interacting NRQCD correlators (similar in spirit to [41, 42] however without taking the thermodynamic limit). These free spectra are obviously devoid of bound state features and hence any peaked structures arising in their Bayesian reconstruction need to be attributed to numerical ringing. Our criterion for accepting a peak as a sign of the presence of a bound state is that it needs to be quantitatively larger than the corresponding wiggly feature in the reconstructed free spectral function[1].

[1] Note that the standard MEM often does not show these ringing structures, since in Bryan's implementation it does not possess enough degrees of freedom to do so. In essence the singular value decomposition deployed there acts as an additional low-pass filter that is applied to the Bayesian solution. This in general however does not mean that the MEM answer resembles the correct spectrum more closely.

III. LOW TEMPERATURE CALIBRATION

β	Volume	T[MeV]	a[fm]	u_0	$M_b a$
6.664	$32^3 \times 32$	52.7	0.117	0.87025	2.76
6.800	$32^3 \times 32$	59.9	0.103	0.874849	2.42
6.950	$32^3 \times 32$	69.0	0.0893	0.879442	2.11
7.280	$48^3 \times 64$	46.6	0.0660	0.88817	1.56

TABLE I. List of parameters for the $T \simeq 0$ lattice configurations, used to calibrate the NRQCD energy shift.

In NRQCD, the heavy quark mass scale is integrated out so that the origin of the energy axis is shifted. To retrieve the physical masses of the bottomonium states from these binding energies computed in the EFT, it is necessary to re-introduce the energy shift. In particular we have

$$M^{\rm exp}_{\Upsilon(1S)} = E^{\rm sim}_{\Upsilon(1S)} + 2(Z_{M_b} M_b - E_0), \qquad (17)$$

where $E^{\rm sim}_{\Upsilon(1S)}$ is the $(1S)$ energy computed in the Υ channel, Z_{M_b} is the mass renormalization, M_b denotes the bare lattice heavy quark mass, while E_0 is an additional energy shift [36]. $M^{\rm exp}_\Upsilon$ refers to the experimental value for the mass of the Υ state. The energy shift and the renormalization factor depend on the lattice cut-off scale. For this reason we introduce a β-dependent energy shift parameter

$$C_{\rm shift}(\beta) = 2(Z_{M_b} M_b - E_0), \qquad (18)$$

that will be determined numerically by matching the calculated Υ mass to its experimental value. Since in this work the simulation temperature is changed by changing the lattice spacing, we measure 100 low temperature correlators using the configurations with parameters listed in table I, in order to determine the ground state peak position of the ${}^3S_1$ channel $E_{\Upsilon(1S)}$.

Figure 1 (top) shows the typical behavior of S-wave (Υ) and P-wave (χ_{b1}) channel correlators. They exhibit, as expected, an exponential fall-off at late Euclidean time, which is manifest in a flattening off of the corresponding effective mass parameter (bottom). This tells us that at these low temperatures the ground state only carries a negligible width and is clearly separated from any other excited state peaks in the spectrum. Hence we can carry out a standard exponential fit to determine the NRQCD ground state masses in each channel.

The Bayesian spectral reconstruction of the $T \simeq 0$ data is performed using at each of the β values the same numerical frequency interval $I_\omega = [-0.5, 30]$ discretized in $N_\omega = 1800$ steps. A high precision interval of $N_{\rm hp} = 550$ points is chosen around the lowest lying peak to resolve its narrow width. The values $\tau_{\max}$ are rescaled, so that in each case the algorithm uses $\tau^{\rm num}_{\max} = 20$. This

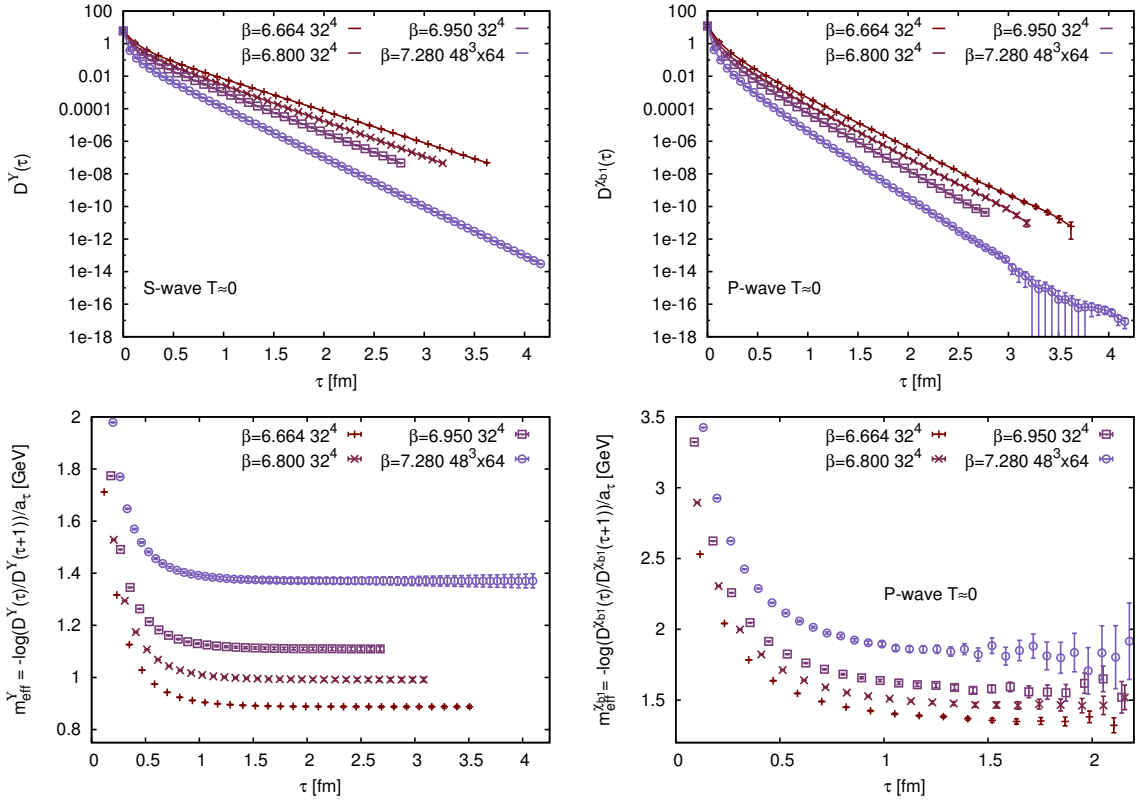

FIG. 1. The lattice NRQCD correlators (top) and corresponding effective masses (bottom) $m_{\rm eff}(\tau) = -\log[D(\tau)/D(\tau+a_\tau)]/a_\tau$ in the S-wave channel (left) and P-wave channel (right) at $T \simeq 0$ for $\beta = 6.664, 6.800, 6.950$, and 7.280

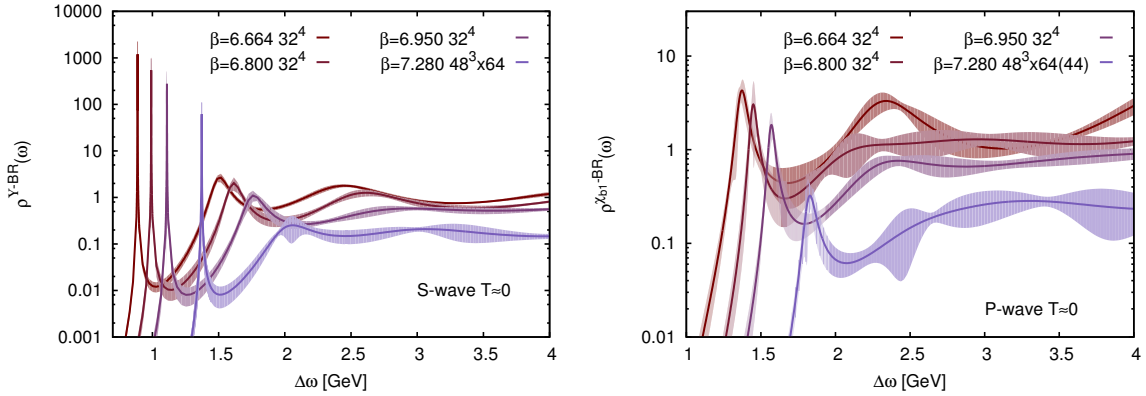

FIG. 2. Bayesian reconstruction of the non shifted spectra in the S-wave channel (left) and P-wave channel (right) $T \simeq 0$ temperature for $\beta = 6.664$ (dark red solid), 6.800 (dashed), 6.950 (solid) and 7.280 (light blue dashed). Note that at $\beta = 7.280$ we only use the first 44 data points there the signal is not yet lost to roundoff-errors.

reduces systematic uncertainties, since each reconstruction proceeds based on the same relation between τ and ω. For $\beta = 7.280$ we discard the last 19 data points, as their values are dominated by noise probably arising from finite rounding errors. Taking a constant default model $m(\omega) = \text{const.}$, which is normalized according to $D(\tau = 0)$ and enforcing the condition $|L - N_\tau| < 10^{-5}$, we find the optimal solution according to Eq. (16) using the LBFGS algorithm. We repeat the reconstruction ten times using in each instance a different set of 90 of the 100 measured correlators and determine from the variation between individual results the Jackknife error-bars shown in the figures below. The arithmetic used in the evaluation of the likelihood and prior probability is taken to be 768 bits. The results of Bayesian reconstruction of the Υ and χ_{b1} spectral functions are shown in Fig. 2. The $\Upsilon(1S)$ is very well determined from the reconstruction. The second bump corresponds to excited states, mostly

$\Upsilon(2S)$. The difference between the position of the first and the second peak is 608, 617, 640 and 664 MeV for $\beta = 6.664,\ 6.800,\ 6.95$ and 7.28, respectively. These values are reasonably close to the experimental value for the $2S-1S$ Υ mass splitting of 563 MeV, and are smaller than the $3S-1S$ Υ mass splitting, which is equal to 895 MeV [32]. The integral under the peak is proportional to the wave function at the origin squared, $|R(0)|^2$. We find that the ratio of the integral of the first peak to the integral of the second peak is about one, whereas the corresponding ratio of $|R(0)|^2$ is expected to be about half [33]. The area under the peak is more affected by contamination from higher states compared to the peak position. This is similar to the situation in the charmonium sector [34].

In the case of P-wave spectral function the first peak corresponding to the $\chi_{b1}(1P)$ state is broader and the statistical errors on the spectral functions are larger. This is due to several effects. First, the mass of the $\chi_{b1}(1P)$ state is larger than the mass of $\Upsilon(1S)$ so the signal-to-noise ratio is smaller. Second, the amplitude of the ground state is proportional to $|R'(0)|^2/M_b^2$ and thus is smaller compared to the S-wave amplitude. In addition the continuum part of the spectral function scales like $\omega^{1/2}$ for the S-wave, while it scales like $\omega^{3/2}$ for the P-wave. As the result the relative contribution of the lowest peak versus the continuum part of the spectral functions is much smaller for P-waves. This makes the reconstruction of the P-wave spectral function more difficult, especially at high temperatures.

Both exponential fitting and the determination of the ground state peak position in the S-wave spectrum give a consistent value for $E_{\Upsilon(1S)}$. Hence we are able to determine the constant, $C_{\rm shift}$,

$$M_{\Upsilon(1S)} = E_{\Upsilon(1S)} + C_{\rm shift}(\beta) \qquad (19)$$

where the experimental value, $M_\Upsilon(1S) = 9.46030(26)$ [32] is used as input, at each lattice spacing. Fig. 3 shows the obtained values of $C_{\rm shift}$, plotted against the lattice coupling β, where $\beta = 6.664$ corresponds to the coupling underlying the lowest temperature lattices ($T = 140$ MeV) and $\beta = 7.280$ that for the highest temperature ($T = 249$ MeV).

Fig. 3 shows that the data points are well described by a linear fit. Hence we use the linearly interpolated values for $C_{\rm shift}$ to calibrate the energy scale in the non-zero temperature runs of Table (II).

With this calibration in place we can check the consistency of our approach by extracting the known vacuum ground state mass of the P-wave channel. To this end we fit the lowest lying spectral peaks shown in the right panel of Fig. 2 with a Lorentzian and shift the obtained value according to Eq. (19). The Jackknifed estimates for $M_{\chi_{b1}}$ obtained at each individual β are in turn fitted with a constant, from which we obtain a χ_{b1} mass of $M_{\chi_{b1}} = 9.917(3)$GeV. The assigned error is understood to represent a combination of the statistical errors due to Jackknife variation and systematic errors from variation between different beta values. This value lies slightly above the PDG value of $M_{\chi_{b1}}(1P) = 9.89278(26)(31)$ GeV [32] but is consistent with the one obtained in another recent lattice NRQCD studies with $N_f = 2+1$ flavors [26], i.e. $M_{\chi_{b1}} = 9.921(15)$GeV.

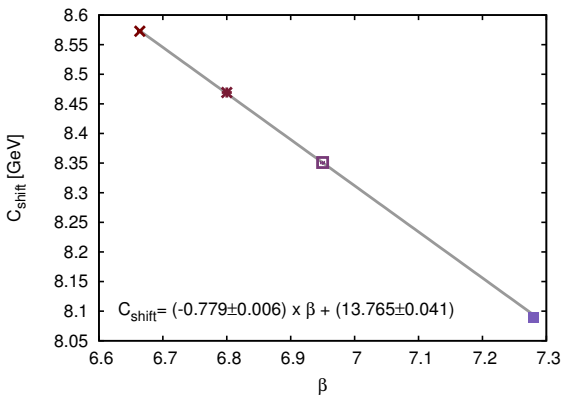

FIG. 3. "Energy shift constant ($C_{\rm shift}$)" determined from the position of the lowest lying peak in the S-wave channel spectral function for $\beta = 6.664, 6.800, 6.950$, and 7.280.

IV. SPECTRAL FUNCTIONS AT FINITE TEMPERATURE

β	T	T/T_c	a(fm)	u_0	$M_b a$
6.664	140	0.911	0.117	0.87025	2.76
6.700	145	0.944	0.113	0.87151	2.67
6.740	151	0.980	0.109	0.87288	2.57
6.770	155	1.01	0.106	0.87388	2.50
6.800	160	1.04	0.103	0.87485	2.42
6.840	166	1.08	0.0989	0.87612	2.34
6.880	172	1.12	0.0953	0.87736	2.25
6.910	177	1.15	0.0926	0.87827	2.19
6.950	184	1.19	0.0893	0.87945	2.11
6.990	191	1.24	0.086	0.88060	2.03
7.030	198	1.29	0.0829	0.88173	1.96
7.100	211	1.37	0.0777	0.88363	1.84
7.150	221	1.44	0.0743	0.88493	1.75
7.280	249	1.61	0.0660	0.88817	1.56

TABLE II. List of parameters for the $T > 0$ lattice configurations used in extracting the in-medium bottomonium spectral functions.

At each of the temperatures listed in Table II, we solve Eq. (3) to obtain 400 estimates of the S-wave and P-wave lattice NRQCD correlators at $N_\tau = 12$ data points. In Fig. 4 the ratio between the finite temperature averaged correlators and their low temperature counterparts

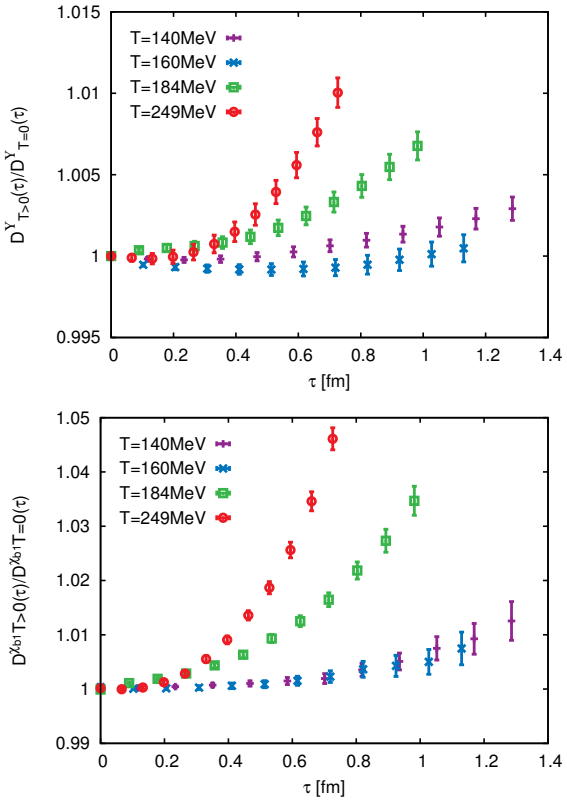

FIG. 4. Ratios of the Euclidean correlator at finite temperature and close to $T = 0$ for the Υ (top) and χ_{b1} (bottom) channel at the lattice spacings, where $T \simeq 0$ measurements were carried out.

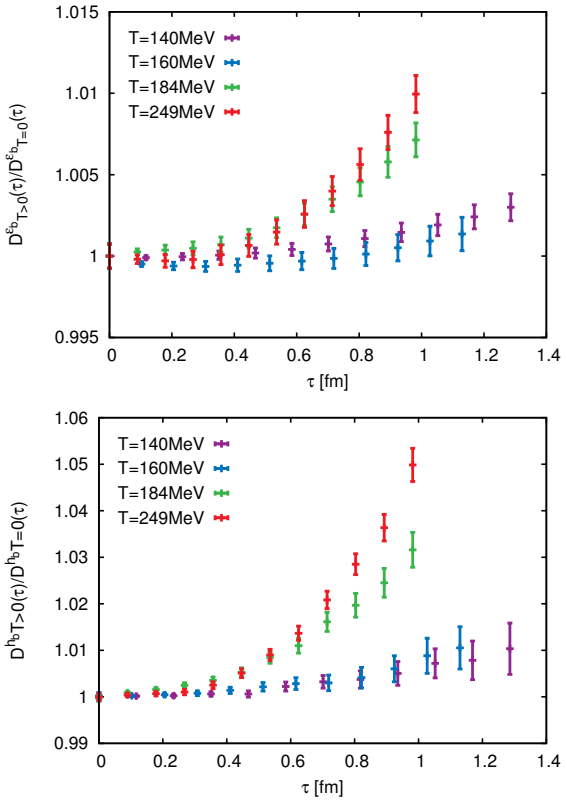

FIG. 5. Ratios of the Euclidean correlator at finite temperature and close to $T = 0$ for the η_b (top) and h_b (bottom) channel at the lattice spacings, where $T \simeq 0$ measurements were carried out. Note the qualitative as well as quantitative similarity to the Υ and χ_{b1} ratios shown in Fig. 4

is plotted for the four lattice spacing at which a $T \simeq 0$ measurement is available. We observe statistically significant in-medium modification of both Υ and χ_{b1} correlators starting at temperature $T_1 = 160$ MeV. While the medium modification for the S-wave leads to changes of at most 1% the P-wave correlators exhibit a stronger effect, i.e. up to 5%. This is expected because the larger size of the χ_{b1} state makes is more susceptible to medium effects. We also calculated the above ratio for $n = 3$ and 4 and found that it is independent of n within the statistical accuracy. Note that we see a smaller modification of the ratio of the correlators compared to previous NRQCD studies [25, 26]. The ratio of the finite and zero temperature correlators for η_b and h_b was also determined and their temperature dependence is shown in Fig. 5. It is similar to that of the Υ and χ_{b1} correlators, respectively. This is expected since the sign and the magnitude of the binding energy of η_b and h_b are almost the same as those of Υ and χ_{b1}.

From the measured correlators, we extract the corresponding spectral functions using both the new Bayesian method and the conventional MEM. The NRQCD energy shift obtained in section III is used to set the absolute physical energy scale.

The Bayesian spectral reconstruction of the $T > 0$ data is performed using at each of the β values a common numerical frequency interval $I_\omega = [-1, 25]$ discretized in $N_\omega = 1200$ steps. A high precision interval of $N_{\rm hp} = 550$ points is chosen around the lowest lying peak to resolve its narrow width. The value $\tau_{\rm max} = 12$ is rescaled, so that in each case the algorithm uses $\tau^{\rm num}_{\rm max} = 20$. Taking a constant default model $m(\omega) = \text{const.}$, which is normalized according to $D(\tau = 0)$ and enforcing the condition $|L - N_\tau| < 10^{-5}$, we find the optimal solution according to Eq. (16) using the LBFGS algorithm. We repeat the reconstruction ten times using in each instance a different set of 360 of the 400 measured correlators and determine from the variation between individual results the Jackknife error-bars shown in the figures below. The arithmetic used in the evaluation of the likelihood and prior probability is taken to be 512 bits.

The MEM reconstructions are performed with almost the same settings, only a different frequency interval $I_\omega = [-0.15, 25]$ is chosen. The reason is related to the restricted nature of the search space, due to which the reconstruction success depends strongly on choosing $\omega_{\rm min}$ close enough to the relevant spectral features (see also the discussion of the MEM systematics in Appendix A). We select an α range that covers the peak in the probability distribution $P[\alpha]$ and due to the absence of true convergence stop the deployed Levenberg Marquardt minimizer

if it reaches a step size of 5×10^{-9}.

A. The Upsilon channel – S-wave

In Fig. 6 we show several different visualizations of the reconstructed S-wave channel spectra for a qualitative inspection. The left column contains the results of the Bayesian reconstruction, while in the right column the MEM results are presented.To obtain an overview of the different orders of magnitude between the ground state peak and higher lying features, the top row figures are given in logarithmic scale spanning the relevant frequencies above the $2M_b$ threshold. All fourteen spectra between 140MeV (dark violet) and 249MeV (red) are included. The middle row compares in linear scale three spectra at the lowest and at the highest temperatures investigated. The bottom row contains the spectra just above the deconfinement transition.

We find that the new Bayesian approach allows us to extract the features of the spectral functions with a much higher resolution than the MEM. Based on exactly the same data set, we manage to obtain a width of the lowest lying peak, which is consistently at least an order of magnitude smaller than that of the MEM. Furthermore we observe that the functional form of the ground state peaks in the MEM resembles a Gaussian. This behavior is qualitatively different from the Lorentzian observed with the new approach, which from general arguments, is expected to be the correct shape for a particle of finite life-time.

If we take a look at the ground state peak reconstructed from the new approach, we see that with increasing temperature there appears to set in a monotonous, albeit relatively small shift of the peak position to higher frequencies as well as a broadening of the width. While it is tempting to attribute these changes to the in-medium modification of bottomonium itself we have to first ascertain how far the systematic uncertainties due to the limited number of data points underlying the reconstruction do influence the outcome.

Two different comparisons help us to understand the limitations of the accuracy of our results. The first is shown in Fig. 7, where we compare the effect of removing all but twelve data points from the $T \simeq 0$ correlator data sets used in the calibration performed in sec. III. Since the Kernel in our case is temperature independent this comparison tells us how the same spectrum encoded at different temperature is resolved by our method[2]. As we can see the accuracy differs for different lattice spacing, the change in mass and width being 2MeV for $\beta = 6.664$ and maximal 31MeV for the width at $\beta = 7.280$.

The second comparison is shown in Fig. 8, where we remove from the $T > 0$ correlator data set itself up to four of the points closest to $\tau_{\max} = 1/T$. We find that the result is a monotonous shift of the reconstructed peak position to higher frequencies and a significant increase in the broadening of the width. Both the influence on the position and width go beyond the error bars shown, which represent the statistical uncertainty and are obtained from the Jackknife variance. The strength of the effects is comparable to those observed in Fig. 7.

From these two checks we conclude that the size of our data set does not allow us to make a quantitative statement about the changes in peak position and width with temperature as the systematic errors dominate our results [3]. We however are in a position, due to the superior resolution of the new Bayesian approach, to give stringent upper limits on the size of the in-medium modification of Υ ranging between

$$\begin{aligned} \Delta m_{\mathrm{T}}(140\mathrm{MeV}) < 2\mathrm{MeV}, \quad \Delta\Gamma_{\mathrm{T}}(140\mathrm{MeV}) < 5\mathrm{MeV} \\ \Delta m_{\mathrm{T}}(249\mathrm{MeV}) < 40\mathrm{MeV}, \quad \Delta\Gamma_{\mathrm{T}}(249\mathrm{MeV}) < 21\mathrm{MeV}. \end{aligned} \tag{20}$$

Another question we can address, is to determine an upper bound for the temperature up to which the Υ channel ground state survives. As we have seen in the previous discussion, the effect of a reduced number of data points is a monotonous broadening of the ground state peak. If a well defined peak is visible in the reconstruction the true spectrum should also possess such a structure of at least the same strength. In that sense Fig. 6 allows us to confirm the qualitative findings of previous lattice NRQCD studies [25, 26] in that the ground state peak retains a narrow width up to the highest temperature studied ($T = 249$ MeV). While the survival of the ground state peak in the S-wave channel is a robust feature of our analysis, no definite statements can be made about the fate of $\Upsilon(2S)$ state due to the systematic errors related to the number of data points and small extent of the time direction. This will become apparent in the discussions below.

The determination of the actual survival or dissolution of the ground state from such an inspection by eye of the lowest lying peak shape of the reconstructed spectra however is highly non-trivial. Indeed it needs to be understood, whether a peak visible in the Bayesian spectra can be attributed to a bound state held together by the strong interactions. Uncertainty here arises from the fact that we reconstruct spectra from a finite number of data points, which will inevitably lead to the presence of numerical ringing. This in turn needs to be distinguished from actual physical peak structures.

[2] Since in the new Bayesian approach the dimensionality of the solution space is not restricted apriori to the number of data points as in the standard MEM, changing the number of underlying data points only affects the amount of information available and does not change the reconstruction prescription.

[3] Note that the default model dependence and other systematic error are smaller than the dependence on N_τ as can be seen in Appendix A

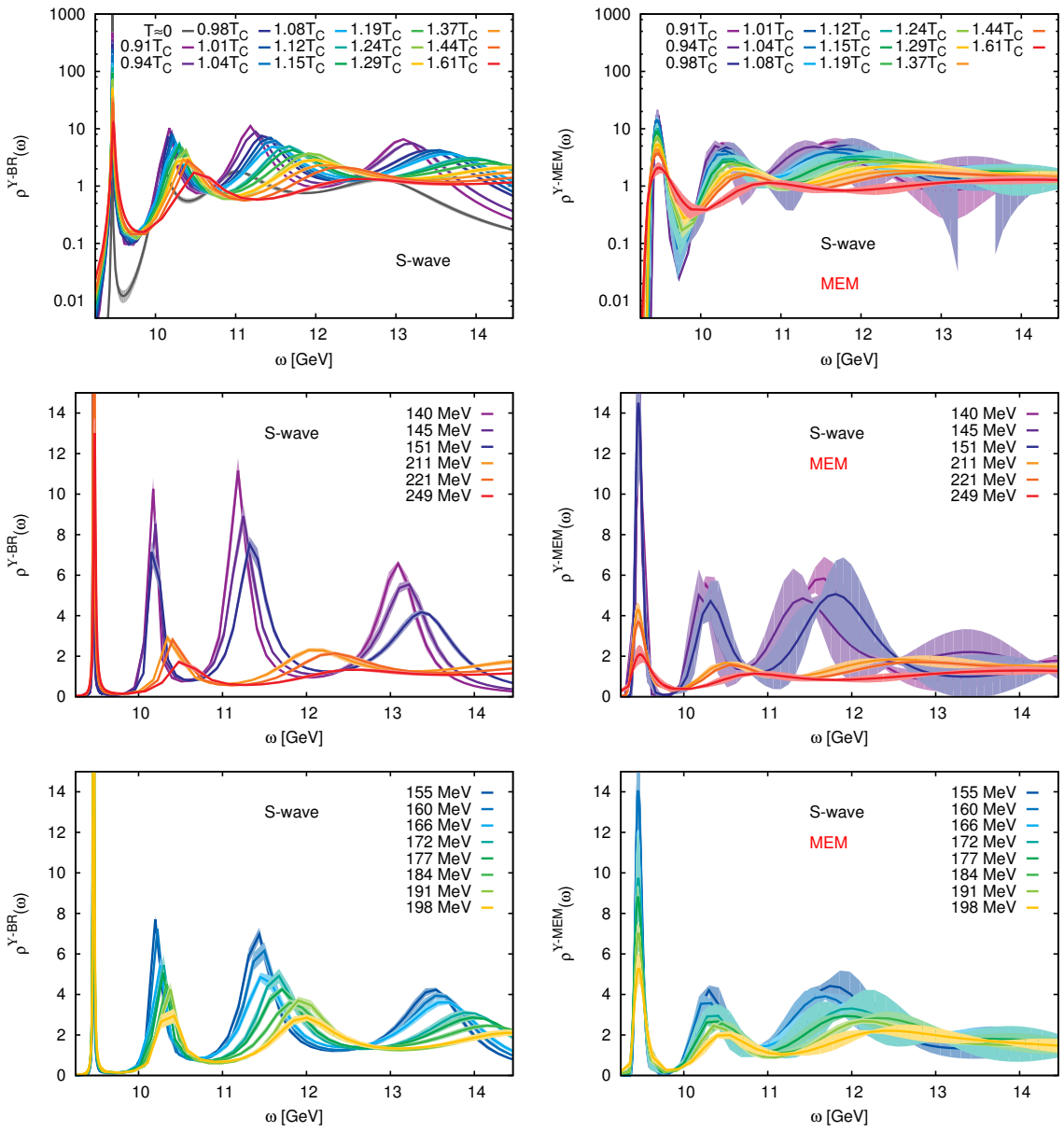

FIG. 6. The mass-shift calibrated S-wave spectra from the new Bayesian approach (left column) and those from the MEM (right column) for fourteen different temperatures between 140MeV (dark violet) and 249MeV (red). The middle row shows spectra for the three lowest temperatures (below T_c) and the three highest temperatures. The bottom figures contain spectra just above the deconfinement transition $T = 155\text{MeV}, \cdots, 198\text{MeV}$. Note that even though on a linear scale the ground state peak from the novel method does not appear to change (bottom left) its height decreases as can be seen in the top left panel.

Here we propose to give the decision about survival or melting a solid footing through a comparison of the fully interacting spectra to those obtained from non-interacting correlators. To this end we set all links on our lattices to unity when calculating the Euclidean NRQCD Green's function. The same random sources as in the interacting case enter the initial conditions for Eq.(3). Since the free correlators are not uniquely defined in lattice NRQCD, it is our choice of $S(\mathbf{x})$ that determines their values at $\tau = 0$. Their time evolution depends on the NRQCD mass parameter $M_b a$, for which we choose the same β dependent values obtained on the interacting lattices we wish to compare to. To enable a meaningful comparison between our reconstructed spectra, we normalize in the following the free correlator at the first time step to the value of the corresponding interacting spectral function. Since the free correlators also possess different, i.e. much smaller errors than the interacting ones, we add Gaussian noise of a similar strength as their errors to the free data points before the reconstruction. Note that spectral functions from free NRQCD correlators do not contain a physical scale. We introduce the scale in

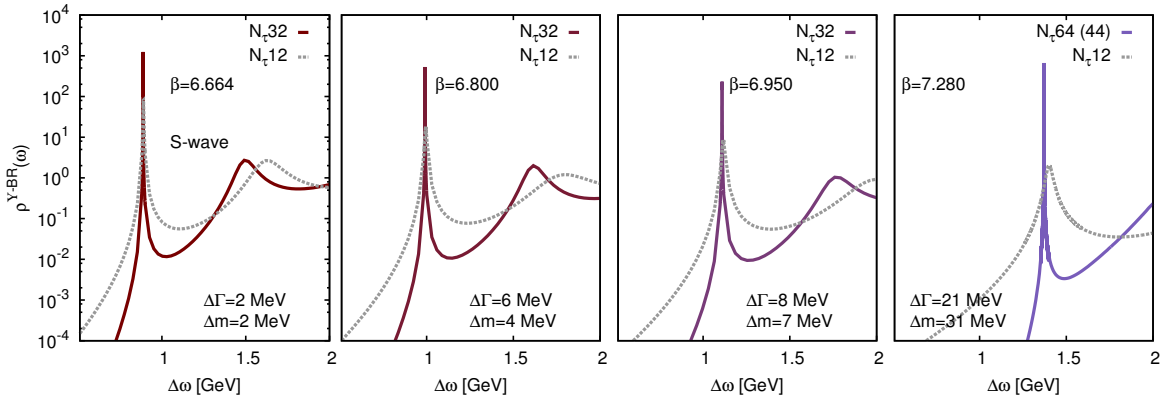

FIG. 7. Change in S-wave peak position and width when reconstructing the $T = 0$ spectra at $\beta = 6.664, \cdots, 7.280$ (from the left to the right) from the full $\tau_{\max} = 32/64$ data set, as well as from the subset with $\tau_{\max} = 12$. Since for a fixed β the high frequency regime remains unchanged when going from $T \simeq 0$ to $T > 0$ the observed differences can serve as a measure of the limits to the reconstruction accuracy.

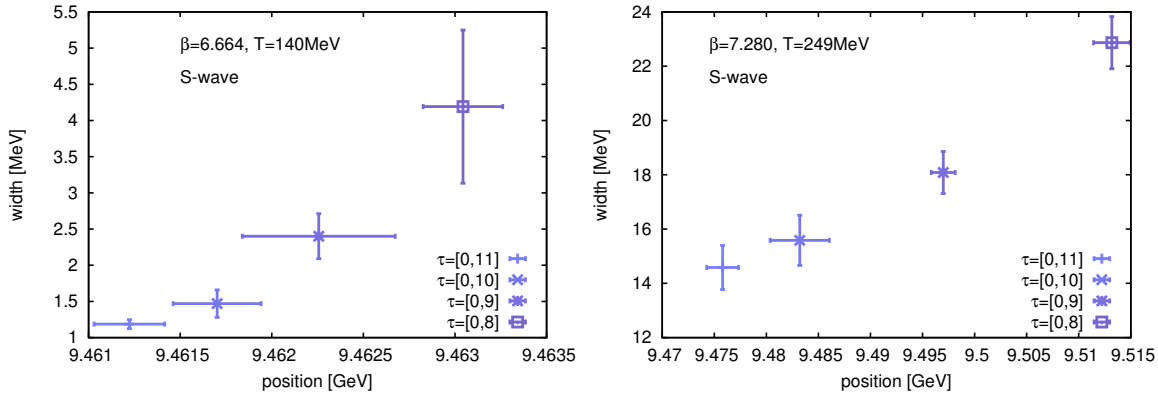

FIG. 8. S-wave at 140MeV (left) and 249MeV (right): Dependence of the reconstructed lowest peak position and peak width on choosing different subsets of data points along the τ axis. Note that the systematic effect of removing data points leads to a shift of the peak width and a broadening of the peak beyond the Jackknife errorbars

the free theory calculation by using the lattice spacing that corresponds to the value of β for which the comparison with free spectral function is performed.

In Fig. 9 we present this comparison in the S-wave channel at the largest (left) lattice spacing $\beta = 6.664$ ($T = 140$MeV) and the smallest (right) $\beta = 7.280$ ($T = 249$MeV). The colored solid curves show the result of the finite T reconstruction from $N_\tau = 12$ data points, while the dark blue, dashed curve represents the reconstruction from the first $\tau_{\max} = 12$ data points of the $T \simeq 0$ correlator. As we discussed before with the limited number of data points available to us, the reconstructed spectra at $T \simeq 0$ and $T > 0$ are very similar especially around the lowest lying peak. On the other hand the free spectra obtained from the same number of data points do differ. The Bayesian reconstructions of the free spectra in Fig. 9 show peak structures even though there are no such features present in the analytic form of free NRQCD spectral function. This is reminiscent of the Gibbs phenomenon mentioned in section II. Here in the case of Υ, the ground state peak at $T > 0$ is easily distinguished from this numerical ringing, as it is at least one order of magnitude larger. From this results we conclude that the ground state of the Υ channel survives at least up to $T = 249$MeV.

For comparison purposes we show in Fig. 10 the interacting (colored gray) and free spectra (gray) obtained from a MEM reconstruction. As we already saw in Fig. 6, the lowest lying peaked features are much more shallow here than in the novel Bayesian approach and their functional form is not Lorentzian, contrary to what is expected for a particle of finite life-time. Consistent with the previous discussion, we find that even at the highest temperature a ground state peak appears to survive. Note that the smoothness of the MEM free spectra does not necessarily mean that an accurate reconstruction has been achieved. Indeed as we increase the number of basis functions to $N_{\text{ext}} = 48$, the number of wiggles, at least for $\beta = 6.664$, significantly increases and the result approaches a similar form as the Bayesian result obtained by the novel method.

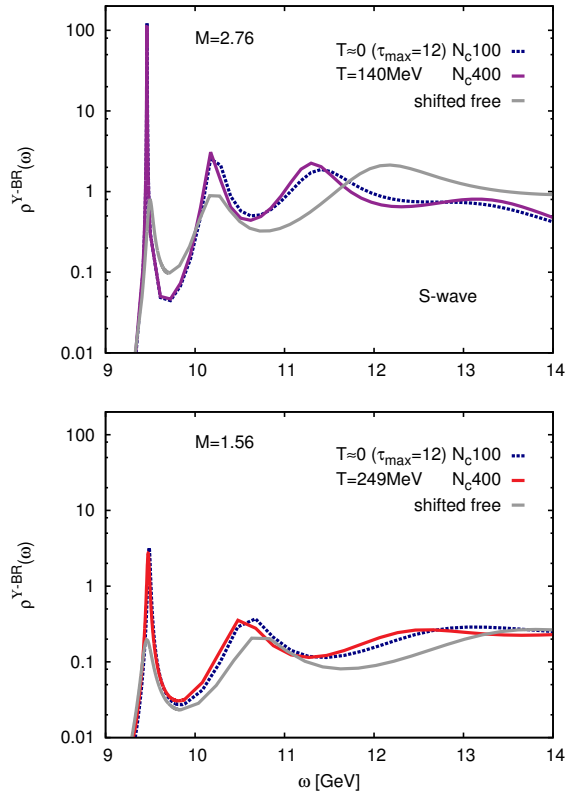

FIG. 9. S-wave spectral reconstructions at $T = 140$MeV (top) and $T = 249$MeV (bottom). To disentangle systematic and medium effects we compare the Bayesian $T > 0$ spectra from all $N_\tau = 12$ data points (colored solid) to the spectra obtained from the first $\tau_{\max} = 12$ points of the $T \simeq 0$ correlator (dashed gray). To verify the presence of a bound state the spectra from non-interacting correlators are plotted (solid gray). N_c denotes the number of correlators used in the analysis.

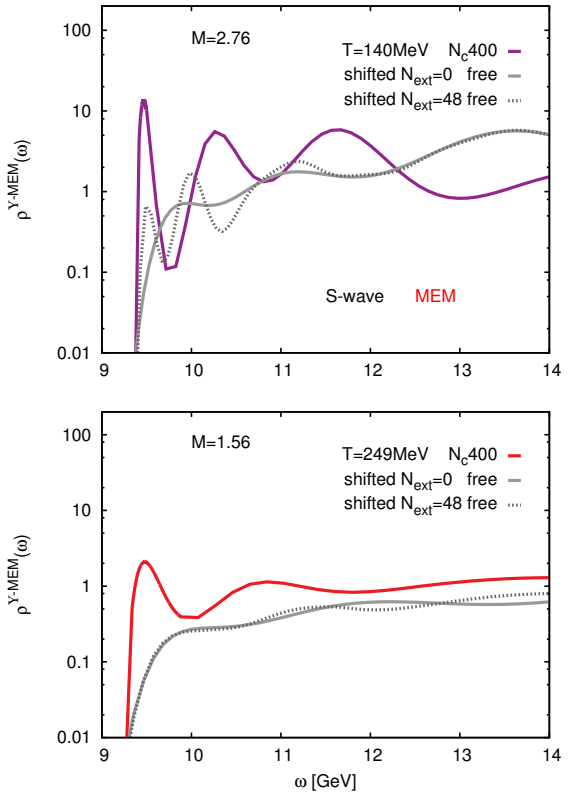

FIG. 10. S-wave MEM spectral reconstructions at $T = 140$MeV (top) and $T = 249$MeV (bottom). Finite T spectrum (colored) as well as free spectrum with standard (solid gray) and extended ($N_{\text{ext}} = 48$) search space (dashed gray).

B. The χ_{b1} channel – P-wave

We continue with the P-wave (χ_{b1} channel) spectral functions shown in Fig. 11, where again the results of the new Bayesian approach on the left are contrasted to the Maximum Entropy Method on the right. The P-wave spectra, due to the larger ground state mass of χ_{b1}, start at higher frequencies and thus the underlying correlators suffer more strongly from the finite number of measurements and lead to less reliable reconstructions, which is reflected in larger error bars. The top row contains the spectral functions at all temperatures, while the middle row shows those from the lowest three (all below T_c) and for the highest three ($T = 211, 221, 249$ MeV) respectively. The bottom row features the spectra just above the phase transition. As for the S-wave, the new Bayesian approach allows us to obtain much sharper resolved peaks than the MEM, using the same data set. This difference turns out to lead to a pronounced qualitative difference in the P-wave case, as can be seen in the middle row of Fig. 11. The MEM spectra at the highest temperatures appear almost featureless, while the new Bayesian approach manages to resolve a well defined ground-state peak. Hence, while a naive inspection by eye in case of the MEM suggests P-wave melting at $T \gtrsim 211$MeV ($= 1.37T_c$), i.e. slightly above the deconfinement temperature ($T_c = 154$MeV), no such conclusion can be drawn from the result of the new Bayesian approach.

The outcome of the MEM is consistent with the findings of other MEM based studies that suggested P-wave melting already at ($T = 201\text{MeV} = 1.09T_c$). However the spectral functions reconstructed using the new Bayesian approach at the same temperatures, show well resolved narrow peak structures and do not hint at melting of the P-wave bottomonium ground state. Perhaps this is not surprising since the limited search space of the standard MEM artificially restricts the resolution of the reconstructed spectra and thus produces only washed out features while the new Bayesian method operates directly in the full search space and hence can produce well-defined peaks.

Before attempting to clarify the fate of the χ_{b1} state, a look at the systematics for the P-wave is in order. We begin with Fig. 12, where we compare the effect of removing all but twelve data points from the $T \simeq 0$ correlator data sets presented in sec.III. The fact that the χ_{b1} state is located at higher frequencies leads to a stronger exponential fall-off in the correlators and thus leads to a smaller signal to noise ratio than that for S-wave with fixed statistics. Thus we expect that discarding data points will affect the outcome of our reconstruction even stronger in the P-wave case, which is also what we find. The change in mass and width is $\simeq 15$MeV at $\beta = 6.664$. At $\beta = 7.280$ the change in mass is 171MeV and the change in width is $\simeq 40$MeV. In Fig. 13 the second pertinent comparison is shown, where we remove from the $T > 0$ correlator data set up to four of the points closest to $\tau_{\max} = 1/T$. Again we find that the result is a monotonous shift of the reconstructed peak position to higher frequencies while the width does not seem to be affected beyond the relatively large Jackknife error bars. We find the strength of these effects to be stronger than those observed in Fig. 12 for the peak position but comparable for its width. From these previous two tests, we conclude that also for the P-wave, the size of our data set does not allow us to make a quantitative statement about the changes in peak position and width as temperature is changed. Even though the modification of the peak position and width are more pronounced than in the S-wave, also our systematic uncertainty is larger. The upper limits for the in-medium modification of χ_{b1} we can provide are

$$\begin{aligned} |\Delta m_{\mathrm{T}}|(140\text{MeV}) < 60\text{MeV}, \quad \Delta\Gamma_{\mathrm{T}}(140\text{MeV}) < 20\text{MeV} \\ \Delta m_{\mathrm{T}}(249\text{MeV}) < 200\text{MeV}, \quad \Delta\Gamma_{\mathrm{T}}(249\text{MeV}) < 40\text{MeV}. \end{aligned} \tag{21}$$

Returning to the question the fate of χ_{b1} at high temperatures, the need for a robust criterion to distinguish a melted state from a bound state is even more evident for the P-wave. Simply looking at the lowest lying peak in Fig. 11 one might conclude melting of χ_{b1} at $T = 249$MeV, since the second peak structure is as large as the ground state feature. To reach a judgment on χ_{b1} on a systematic basis, we deploy the same strategy as laid out for the S-wave, i.e. comparing the interacting reconstructed spectra to those from free NRQCD correlators with the same bottom quark mass parameter. In Fig. 9 we present such a comparison for the P-wave channel at the lowest temperature (left) $T = 140$MeV ($\beta = 6.664$) and the highest (right) $T = 249$MeV ($\beta = 7.280$). While the colored solid curves represent the result of the finite T reconstruction from $N_\tau = 12$ data points, the dark blue, dashed curve represents the reconstruction from the first $\tau_{\max} = 12$ data points of the $T \simeq 0$ correlator. Just as in the S-wave case, the reconstructed interacting spectra at $T \simeq 0$ and $T > 0$ are very similar. Nevertheless at the lowest temperature $T = 140$MeV distinguishing between the ground state peak and the numerical ringing in the free spectra poses no difficulty, as their amplitudes differs by almost two orders of magnitude. At the highest temperature $T = 248$MeV we find that the reconstructions take on similar values at frequencies above $\omega = 13.5$GeV but a significant difference (at least a factor of three) remains for the lowest lying peak. We have checked that another choice of default model used in the reconstruction of the free spectra do not change the lowest lying peak significantly, as shown in Appendix A. Based on the outcome of this systematic comparison we can establish the survival of the χ_{b1} state up to at least a temperature of $T = 248$MeV.

We close this section with a comparison of the MEM reconstruction of the interacting (colored gray) and free spectra (gray) for the P-wave shown on the right hand side of Fig. 15. As was already found in Fig. 6, the lowest lying peak is very shallow even at the lowest temperature $T = 140$MeV and completely absent at $T = 248$MeV. The

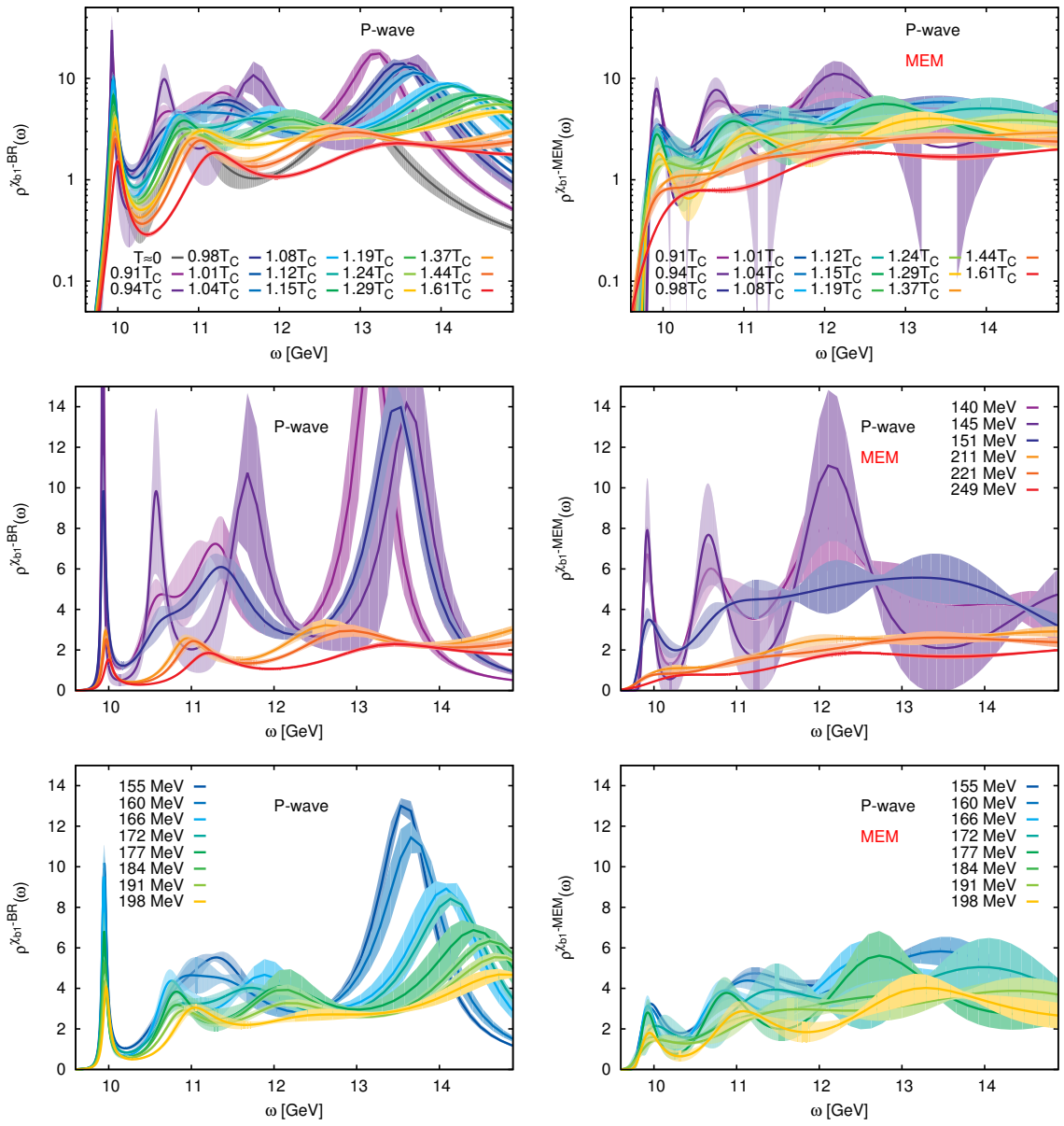

FIG. 11. The mass-shift calibrated P-wave spectra from the new Bayesian approach (left column) and those from the MEM (right column) for fourteen different temperatures between 140MeV (dark violet) and 249MeV (red). The middle row shows spectra for the three lowest temperatures (below T_c) and the three highest temperatures. The bottom figures contain spectra just above the deconfinement transition $T = 155\text{MeV}, \cdots, 198\text{MeV}$.

combination of a lower signal to noise ratio together with the small number of available data points does not allow the MEM to show oscillating behavior even if the number of basis functions is increased to $N_{\text{ext}} = 48$. Hence, although there seems to persist a difference at high T between the free and interacting spectra between 9.5GeV and 11GeV, the limited resolution of the MEM for the interacting spectrum does not allow us to relate it to a surviving χ_{b1} state.

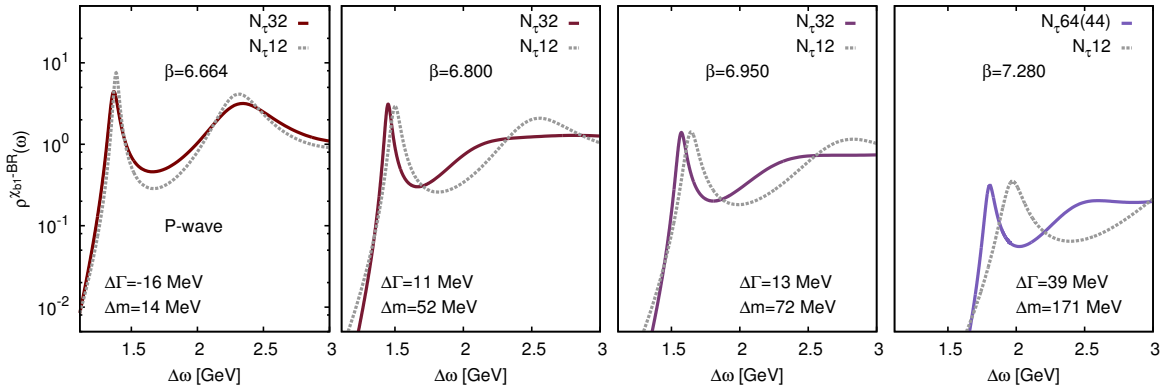

FIG. 12. Change in P-wave peak position and width when reconstructing the $T = 0$ spectra from the full $\tau_{\max} = 32/64$ data set, as well as from the subset with $\tau_{\max} = 12$. Since for a fixed β the high frequency regime remains unchanged when going from $T \simeq 0$ to $T > 0$ the observed differences can serve as a measure of the limits to the reconstruction accuracy.

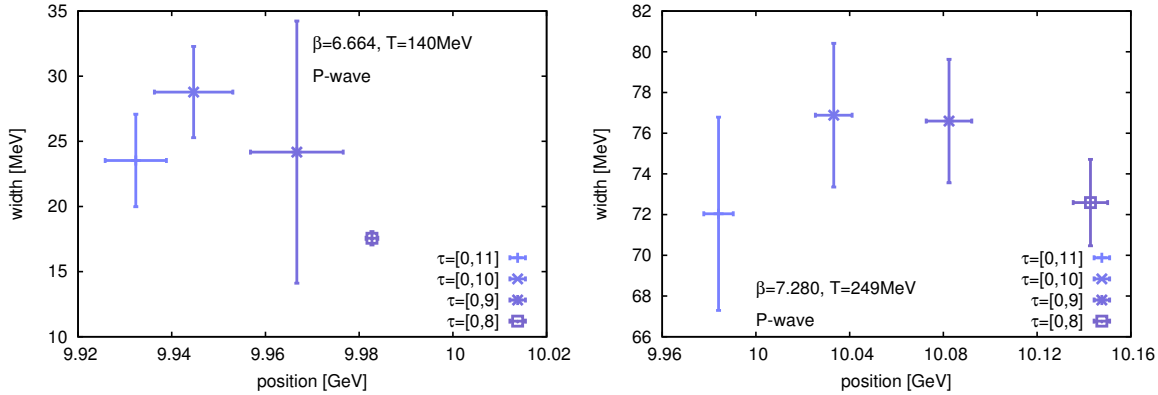

FIG. 13. 140MeV (left) and 249MeV (right): Dependence of the reconstructed lowest peak position and peak width on choosing different subsets of data points along the τ axis. For the P-wave with worse signal to noise ratio, removing data points leads to an even stronger systematic shift of the peak width and a broadening of the peak than in the S-wave case.

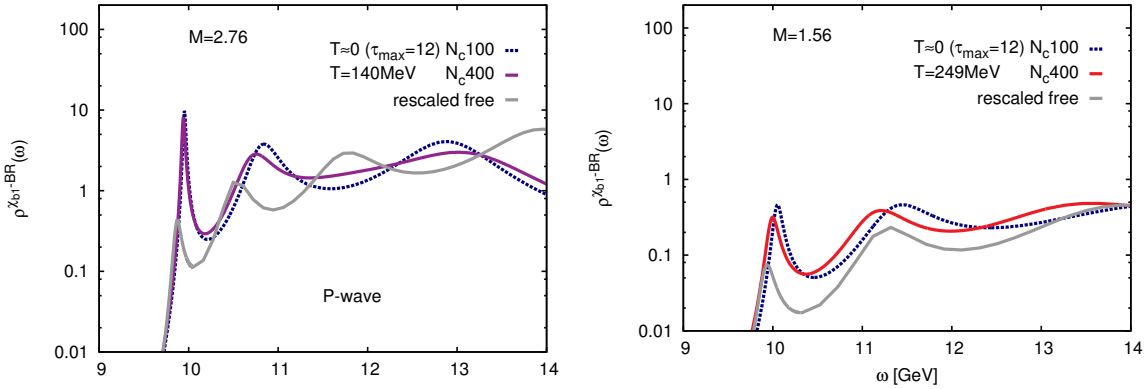

FIG. 14. P-wave spectral reconstructions at $T = 140$MeV (left) and $T = 249$MeV (right). To disentangle systematic and medium effects we compare the Bayesian $T > 0$ spectra from all $N_\tau = 12$ data points (colored solid) to the spectra obtained from the first $\tau_{\max} = 12$ points of the $T \simeq 0$ correlator (blue dashed). To verify the presence of a bound state the spectra from non-interacting correlators are plotted (solid gray).

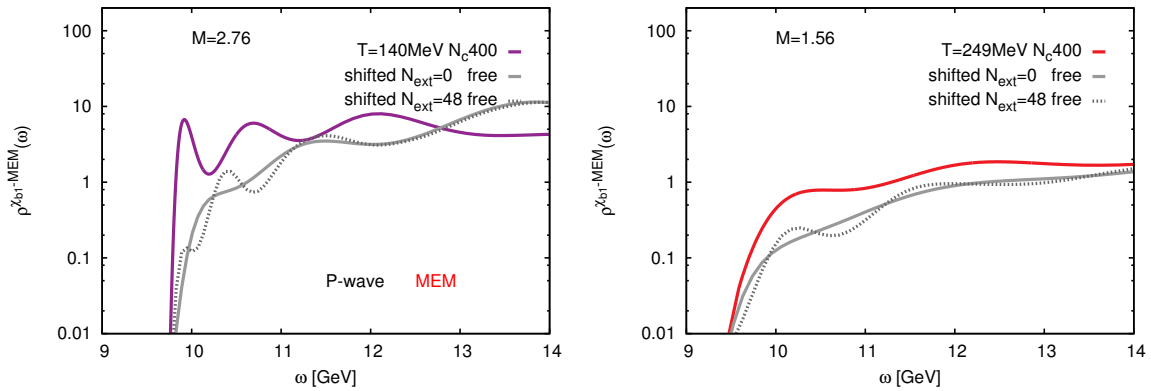

FIG. 15. P-wave MEM spectral reconstructions at $T = 140$MeV (left) and $T = 249$MeV (right). Finite T spectrum (colored) as well as free spectrum with standard (solid gray) and extended ($N_{\rm ext} = 48$) search space (dashed gray).

V. CONCLUSION

The in-medium modification of heavy quark bound states, elucidated by lattice QCD methods, provides first principles insight into the physics of the strong interactions under extreme conditions. Due to the role of bottomonium as probe for the QGP in relativistic heavy-ion collisions, understanding bottomonium behavior in the presence of a thermal medium is of direct phenomenological relevance. In this study we investigated the spectral properties of the Υ ($^3S_1$) as well as the χ_{b1} ($^3P_1$) channel at fourteen different temperatures around the deconfinement transition 140MeV($= 0.911T_c$) $\leq T \leq$ 249MeV($= 1.61T_c$) in a medium with $N_f = 2+1$ light quark flavors.

The underlying $48^3 \times 12$ isotropic lattices were provided by the HotQCD collaboration and are based on the HISQ action. Since temperature is changed by varying the lattice spacing, a narrowly spaced temperature scan was achieved. However, a zero temperature calibration of the absolute energy scale at each lattice spacing was required and has been performed. A lattice regularization of the effective field theory (NRQCD) was deployed to calculate the bottomonium correlators. This allows us to utilize the full number of data points in temporal direction, since the periodic boundary conditions of relativistic field theory are absent. The relation between correlator and spectrum in this case reduces to a convolution over a simple exponential kernel.

We extracted spectral information both with the standard MEM and a recently developed Bayesian approach. This novel method differs significantly from the MEM, and features a prior functional which enforces the positive definiteness of the spectrum, independence of the end result from the choice of units for ρ and favors smooth spectra for the energy region where data does not imprint peaked structures. As a general observation we find that the spectra reconstructed using the new Bayesian approach are far superior to those produced by the MEM as seen in Fig. 6 and Fig. 11. Not only are we able to resolve much narrower peak widths but the functional form of the bound state peaks is reproduced in Lorentzian form, as expected for a particle of finite lifetime. We see by systematically investigating the effect of removing data points in Fig. 7, Fig. 8 and Fig. 12, Fig. 13 that our current data set does not allow us to quantitatively disentangle the effects of the medium from the degradation of the reconstruction quality due to a smaller extent in τ. Nevertheless, due to the high resolution of the new Bayesian approach we are able to give stringent upper bounds on the in-medium modification of both Υ and χ_{b1} states.

From a systematic comparison of the reconstructed spectra from finite temperature correlators to those reconstructed on non-interacting lattices we furthermore conclude that the ground state Υ survives up to at least $T = 249\text{MeV}(= 1.61T_c)$, the highest temperature investigated. A similar comparison carried out for the P-wave channel shows that even though the deviation between interacting ground state peak and numerical ringing in the free spectra is smaller, even at 249MeV at least a factor of three difference between the interacting spectra and the free spectra remains. This suggests to us the survival of the ($^3P_1$) bottomonium ground state up to this temperature (well into the QGP phase).

The conclusion on the S-wave ground state survival agrees qualitatively with those obtained by the MEM. However the restricted search space of the MEM does not allow us to find a well defined peak for the ground state in the χ_{b1} channel at the highest three temperatures. Since the new Bayesian approach is not affected by this well known deficiency of the standard MEM (i.e. changing $\omega_{\min}$ to larger negative values leads to a systematic broadening and eventual disappearance of any reconstructed peaked structures), we are confident that the observed presence of the P-wave peak up to 249MeV is not an artifact due to the spectral reconstruction method.

We have checked that our findings do not suffer from a possibly inadequate choice of lattice NRQCD discretization by repeating the analysis for the values of the parameter $n = 2, 3$ and 4 described in Appendix B. While the high frequency behavior of both the free and the fully interacting spectra do change as expected, we confirm that the ground state peak and its features remain virtually unchanged.

We also investigated additional systematic uncertainties of the spectral reconstruction itself in Appendix A and find that they are in general smaller than the errors introduced due to the finite number of data points. These dependencies appear stronger than what has been found in previous MEM studies. This however is related to the fact that the new Bayesian approach is able to resolve much narrower structures and thus does not hide the default model dependency in an artificially broad reconstructed width.

The results obtained here from the combination of NRQCD correlators and the new Bayesian method are promising. It appears that deficiencies of the MEM can be overcome at least in principle, while the small number of data points still precludes us from a quantitative determination of possible in-medium mass shifts and a width broadening. Carrying out dynamical lattice QCD simulations with a larger number of temporal lattice sites, be it in an isotropic or anisotropic setting are thus called for.

Incremental progress on the reconstruction of spectra can be expetced within the ongoing programs for gauge configurations generation, i.e. $N_\tau = 16$ or $N_\tau = 24$. For a quantitative determination of the in-medium modification, especially the width broadening, it will be necessary to start a dedicated generation program using anisotropic lattices with $N_\tau > 64$. Once the temporal extend becomes as large as $N_\tau > 64$ the default model dependence will also reduce significantly, as the high frequency regime, encoded in the correlator at small τ is more highly resolved. Due to the fact that the reconstruction success depends on the physical temporal ex-

tend, what exact number of of lattice points are needed will ultimately be connected to the melting temperature of the individual state.

We hope that the availability of the new Bayesian approach for the determination of heavy quarkonium in-medium spectral features will benefit the understanding of bottomonium suppression in heavy-ion collision and look forward to future studies with lattices of larger temporal extent and higher statistics.

ACKNOWLEDGMENTS

A.R. thanks Y. Burnier for many fruitful discussions. SK is supported by the National Research Foundation of Korea grant funded by the Korean government (MEST) No. 2010-002219 and in part by NRF-2008-000458. PP is supported by U.S.Department of Energy under Contract No.DE-AC02-98CH10886. AR was partly supported by the Swiss National Science Foundation (SNF) under grant 200021-140234.

Appendix A: Tests of the Bayesian Spectral Reconstruction

Any reconstruction of $N_\omega \gg N_\tau$ parameters from a noisy set of N_τ data points through an inversion of Eq. (10) remains an ill-defined problem. Besides the obvious fact that the results depend on the properties of the measured data itself (i.e. the number of available data points and their signal to noise ratio), we have to control how the inclusion of prior information affects the final outcome. Prior information enters implicitly e.g. through the choice of the underlying frequency interval, as it spans only the region we deem relevant for the spectral function we wish to reconstruct. Explicit prior information on the other hand enters through the choice of prior functional S and the default model $m(\omega)$ it contains. In the following, all of these factors are considered and are independently varied to estimate the systematic uncertainties of the reconstructed spectral function. The main outcomes of these tests are that

- The reconstruction of the ground state peak suffers most from discarding points close to $\tau = \beta$. We however do not observe any abrupt changes when including or discarding the last data point at $\tau = \beta - a_\tau$ in contrast to other studies.
- the ground state peak of the χ_{b1} spectra in general suffers more strongly from the systematic uncertainties, as the signal to noise ratio of the corresponding correlator is consistently smaller than in the Υ case. ($M_{\chi_{b1}} > M_\Upsilon$)
- the size of the statistical error on the correlator data limits how well we can reconstruct the width of the ground state peak. However, with the inclusion of more than $N_{\rm conf} = 360$ configurations for the averaging, the dependence on $N_{\rm conf}$ appears to be small.
- the dependence on the choice of $\omega^{\rm num}_{\rm max} = \omega_{\rm max} a$ (a is the lattice spacing) is small as long as the interval is chosen large enough $\omega^{\rm num}_{\rm max} > 20$ to accommodate all relevant peak structures. The dependence on $\omega_{\rm min} a$ is a bit more pronounced, especially if not enough frequencies in the negative range are included (this dependence is significantly smaller than that in the case of the MEM, where no stable plateau is found).
- using different default models gives roughly twice of the Jackknife error-bar to the first peak position in Υ spectral function and ten times uncertainty to the first peak width. In the χ_{b1} case, due to a worse signal to noise ratio, already default model effect on the peak position may be a factor of eight larger than the statistical errors.

Finally we also take a look at the systematics of the MEM, specifically the fact that that reconstruction success depends strongly on the choice of frequency interval. Indeed we find that simply moving $\omega_{\rm min}$ to larger negative values melts any otherwise visible peaked structures.

Dependence on the τ range

Using a relatively small number of data points, $N_\tau = 12$, we expect the reconstructed spectral function to suffer significantly from removing even more of them. We find as elaborated on in the main text that since low frequency structures dominate late τ times, removing data points close to $\tau = N_\tau$ indeed leads to a significant increase in reconstructed peak width beyond the statistical errorbars as well as a systematic shift of the extracted peak position to larger values as can be seen in Fig. 16 and Fig. 17. On the other hand it is also clear that we do not observe any abrupt changes in the reconstruction if the last data point is included, as has been reported by previous studies.

Dependence on the signal to noise ratio

In contrast to the Fourier transform, where the signal to noise ratio strongly affects the highest possible frequency one can resolve, the inverse Laplace transform reacts to degrading signal with increasing peak widths. Thus a systematic trend towards smaller reconstructed widths is expected if more and more configurations contribute to the averaged underlying correlator. Such kind of behavior can be found for the smallest numbers of used configurations but eventually it seems that a stable plateau is reached at least for the Υ channel (we choose a number of Jackknife bins N_J and reconstruct the spectra for each of these with a corresponding number

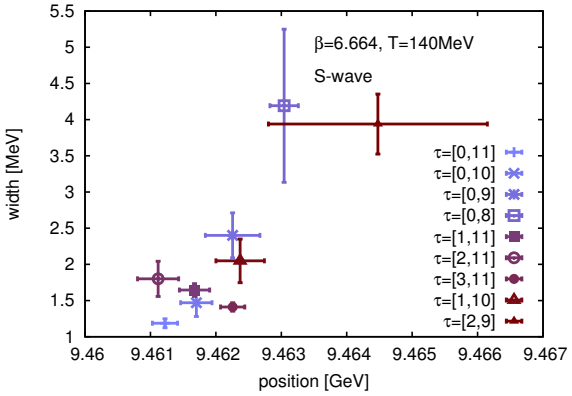

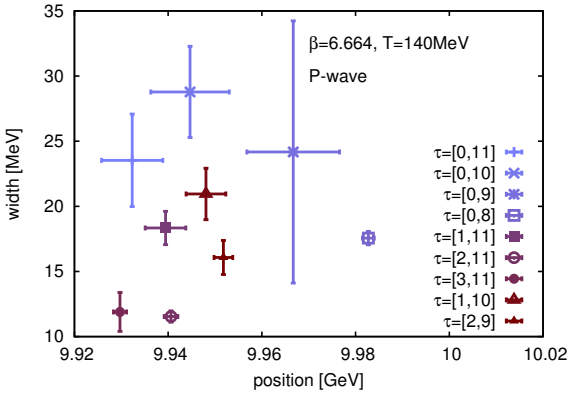

FIG. 16. At 140MeV: Dependence of the reconstructed lowest peak position and peak width on choosing different subsets of data points along the τ axis. In general the peak position is less susceptible than the peak width with the Υ (top) showing consistently less dependence than the χ_{b1} (bottom).

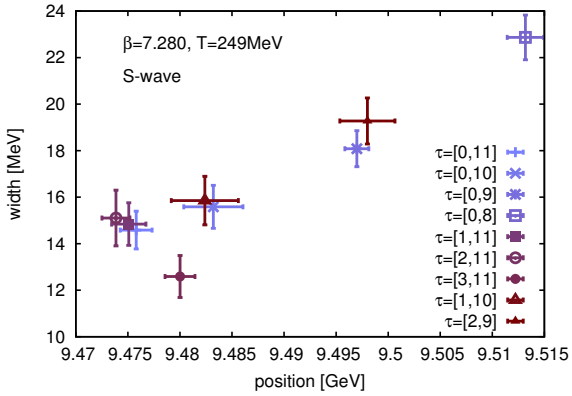

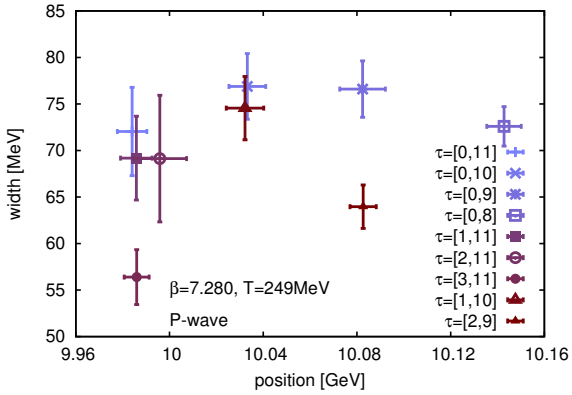

FIG. 17. At 249MeV: Dependence of the reconstructed lowest peak position and peak width on choosing different subsets of data points along the τ axis. In general the peak position is less susceptible than the peak width with the Υ (top) showing consistently less dependence than the χ_{b1} (bottom).

of $N_{\rm conf} - N_{\rm conf}/N_J$ configurations. The peak positions and widths for each bin are plotted against the number of configurations in Fig. 18-Fig. 21). The reconstruction of the peak position in the Υ channel is robust, while in the χ_{b1} channel one can see a slight dependence on the number of used configurations with a trend to lower values.

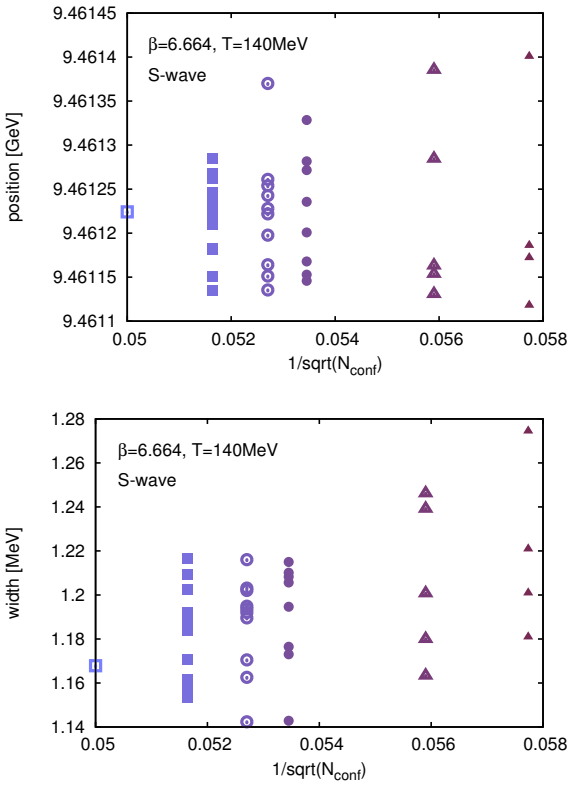

FIG. 18. At 140MeV: The raw Υ reconstructed peak positions (top) and peak widths (bottom) for different choices of the number of Jackknife bins and thus of the number of measurements contributing to the correlator average. Each plotted point corresponds to one spectral reconstruction for an individual Jackknife bin. Their spread is a direct measure of the statistical uncertainty and reduces slightly with increasing number of Jackknife bins. No systematic trend appears in reconstructed peak position, while the peak width seems to move to a smaller value until a plateau is reached at $N_{\rm conf} = 350$.

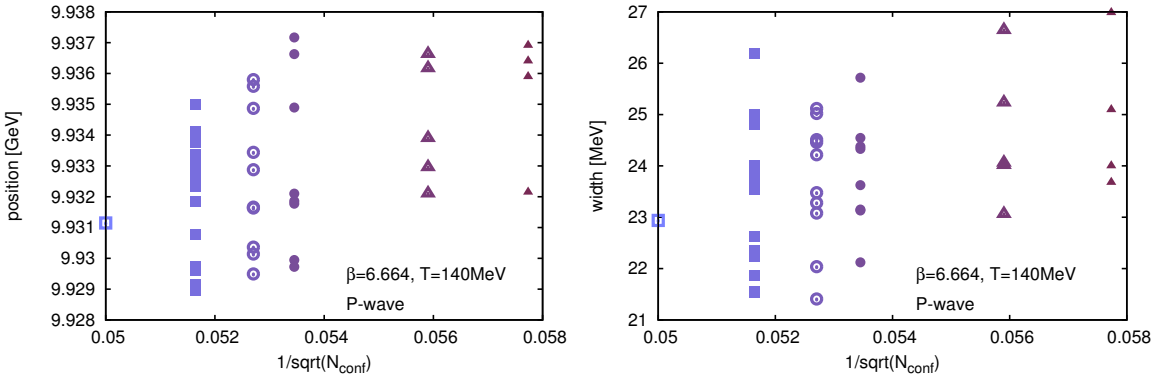

FIG. 19. At 140MeV: The raw χ_{b1} reconstructed peak positions (left) and peak widths (right) for different choices of the number of Jackknife bins and thus of the number of measurements contributing to the correlator average. A slight trend to smaller values of the reconstructed peak position is visible, which however lies within the statistical uncertainty. No systematic trend appears for the peak width.

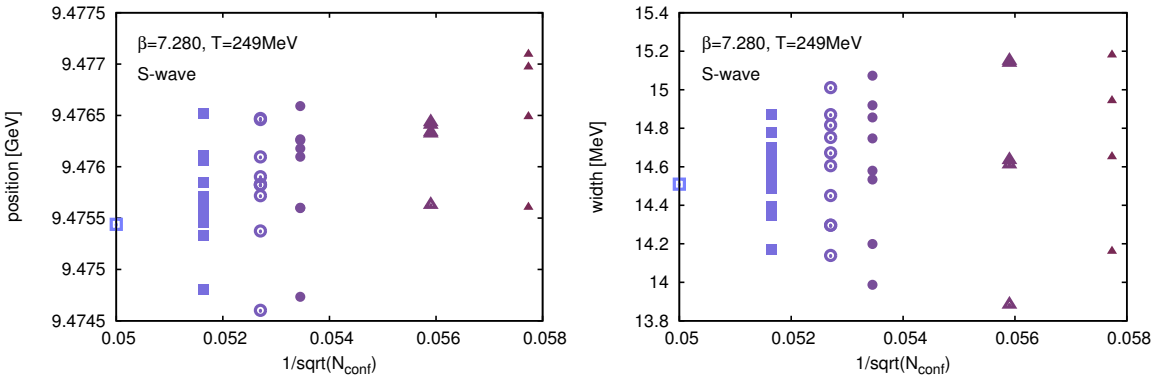

FIG. 20. At 249MeV: The raw Υ reconstructed peak positions (left) and peak widths (right) for different choices of the number of Jackknife bins and thus of the number of measurements contributing to the correlator average. No systematic trend appears in reconstructed peak position and width. In the reconstructed width the reduction of statistical uncertainty with increasing number of used measurements is clearly visible.

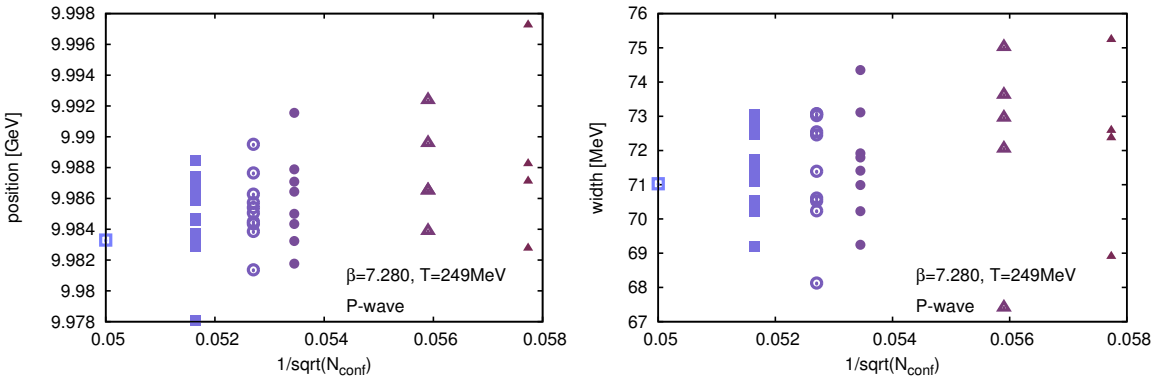

FIG. 21. At 140MeV: The raw χ_{b1} reconstructed peak positions (left) and peak widths (right) for different choices of the number of Jackknife bins and thus of the number of measurements contributing to the correlator average. A slight trend to smaller values of the reconstructed peak position is visible, which however lies within the statistical uncertainty. No systematic trend appears for the peak width.

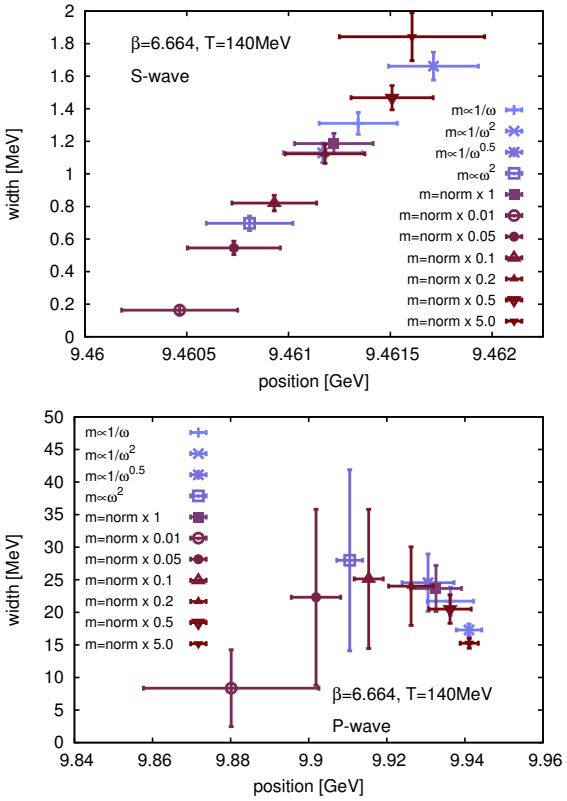

FIG. 22. At 140MeV: Dependence of the reconstructed peak position and width on different choices of the default model for the Υ (top) and χ_{b1} (bottom) channel. Changing the functional form has a similar effect than moderately changing the overall normalization.

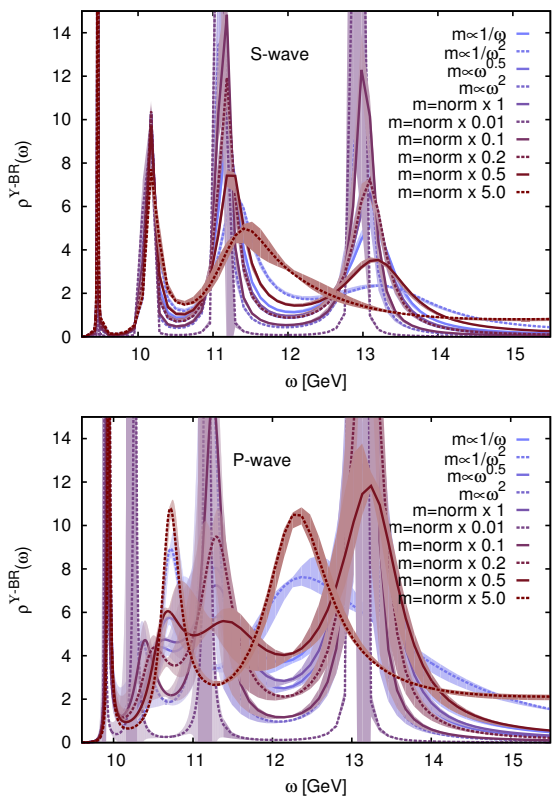

FIG. 23. At 140MeV: The actual spectral reconstructions for each of the choices of the prior model from which the values in Fig. 22 have been determined. The S-wave is shown on the left, the P-wave channel on the right.

Dependence on the default model

The explicit dependence of the finite temperature spectral reconstructions on prior information can be assessed by changing the default model residing in the prior functional S. We change either the functional form $m(\omega) \propto \omega^k$ with $k = \{-1, -2, 0.5, 2\}$, while leaving the normalization intact or change the overall magnitude of the previously normalized constant prior by one of the factors indicated in Fig. 22 and Fig. 24. Note that in the derivation of the prior functional S the constant prior was singled out as being the most neutral default model.

We find that there is a significant dependence of the reconstructed peak position and width on the choice of default model, by which we mean that the induced changes go beyond the statistical error-bars estimated from the Jackknife. For the Υ channel peak position this systematic uncertainty amounts to up to twice the statistical error-bars, while for the width it can be a factor of ten. In the P-wave channel we have a worse situation, since the lower signal to noise ratio leads to the systematics of the peak width being around eight times that of the Jackknife errors while the position only shows a factor of four.

In the case of changing the normalization of the constant prior, the P-wave shows a sudden change once the artificial prefactor reaches 0.01 (Fig. 23 and Fig. 25). In this case three rather sharp peaks appear, which are not found with any other choice of default model. This outcome is the combined result of the weak constraint of the result by the data and the corresponding stronger influence of the prior functional. If the normalization of $m(\omega)$ is changed away from the correct value more than two orders of magnitude the prior probability functional S will favor spectra with much less integrated area as encoded in the data and the accuracy of the reconstructed peak structure suffers. In the S-wave case the dominance of the likelihood due to a better signal to noise ratio prevents the incorrect normalization to distort the final outcome within the parameter tested here. Note that it is however always possible to choose numerical parameters for $m(\omega)$ such that they are highly incompatible with the data and will lead to a distorted reconstruction.

These systematic dependencies appear stronger than what was previously found in the MEM. This is not surprising since the limited number of available degrees of freedom in the MEM washes out features that we are able to resolve with the new method. Consequently the de-

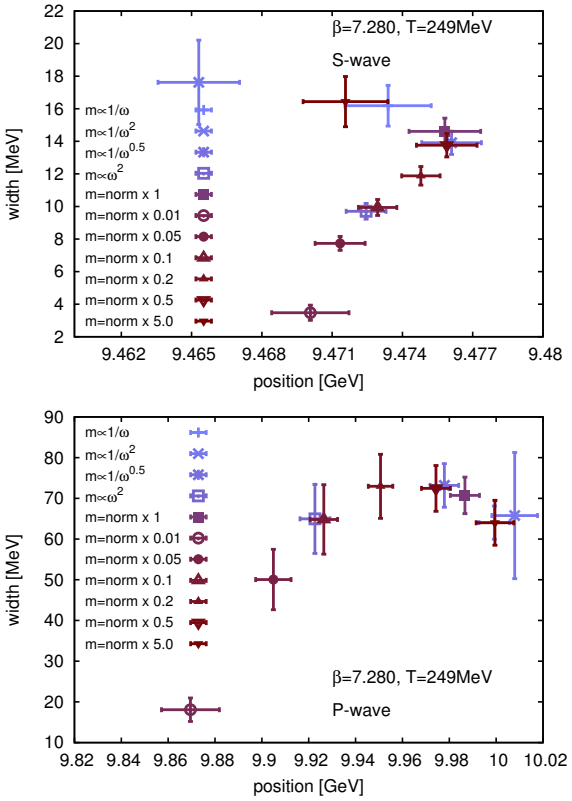

FIG. 24. At 248MeV: Dependence of the reconstructed peak position and width on different choices of the default model for the Υ (top) and χ_{b1} (bottom) channel. Changing the functional form has a similar effect than moderately changing the overall normalization.

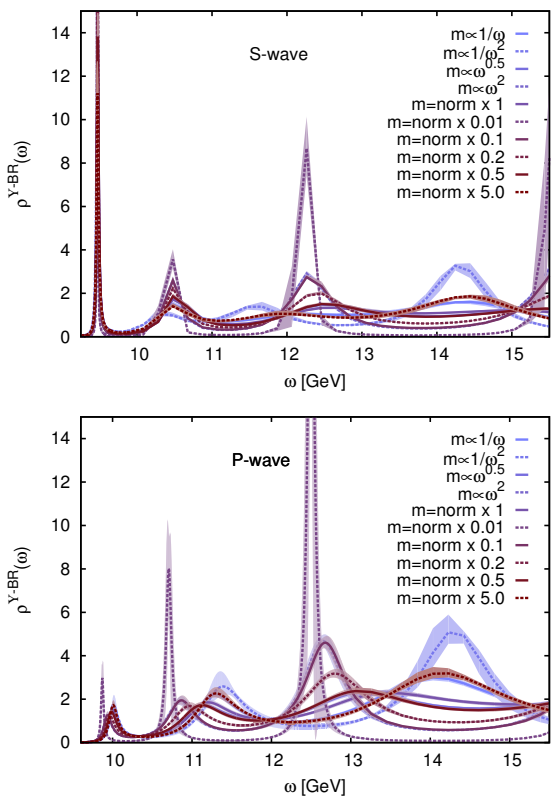

FIG. 25. At 248MeV: The actual spectral reconstructions for each of the choices of the prior model from which the values in Fig. 24 have been determined. The S-wave is shown on the left, the P-wave channel on the right.

fault model dependence is hidden from the MEM inside e.g. the larger widths, which make the result appear robust against changes in $m(\omega)$ but do not allow to assign a high accuracy.

For the determination of possible ground state survival or melting, we compare the interacting spectral functions to those from free NRQCD correlators. For this test to be meaningful we also need to understand the default model dependence of the free spectra. In Fig. 26 we show the reconstructions of the free S-wave spectra based on a similar selection of default models deployed in the finite temperature case above. We find that while the higher lying wiggly features depend on the form of $m(\omega)$ the lowest lying peak is quite stable. In the case of the free P-wave spectra shown in Fig. 26 we see that the lowest peak is slightly more susceptible to a change in the default model, its shape is however robust enough for our conclusion about a difference between interacting and free spectrum at $T = 249$MeV to hold.

The fact that the lowest lying artificial ringing structures are stable against default model changes should not be disconcerting. Similar to the Fourier transform, the presence and strength of the Gibbs ringing depends solely on the number of available data points. Adding noise might wash out some of these features or make them more susceptible to the form of the default model but with the size of the statistical errors used here, the lowest lying wiggle indeed remains stable.

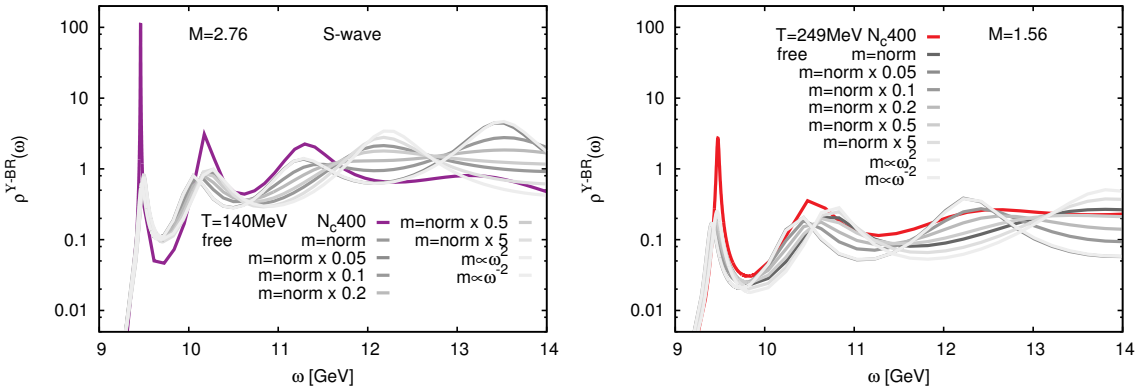

FIG. 26. Free S-wave spectra (gray) for different choices of the default model $m(\omega)$, reconstructed from non-interacting NRQCD correlators using the effective mass values from the $T = 140$MeV (left) and $T = 249$MeV (right) lattices. In addition the interacting spectrum at the same temperature is shown (colored solid).

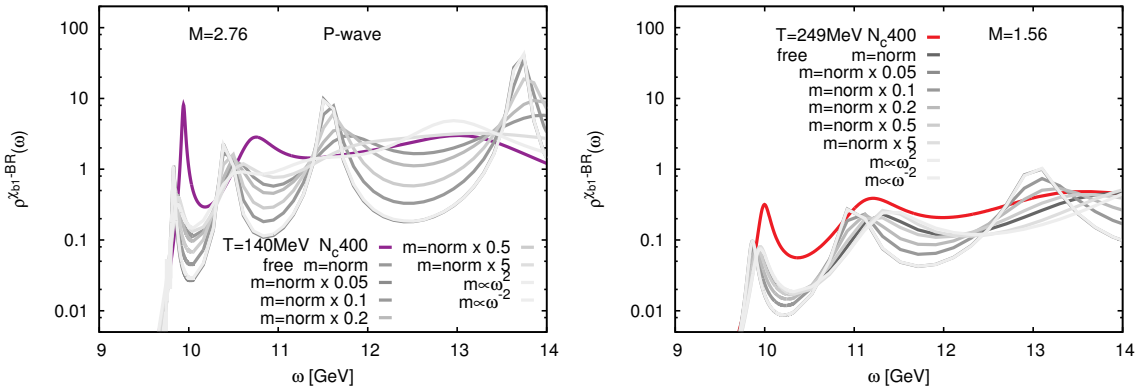

FIG. 27. Free P-wave spectra (gray) for different choices of the default model $m(\omega)$, reconstructed from non-interacting NRQCD correlators using the effective mass values from the $T = 140$MeV (left) and $T = 249$MeV (right) lattices. In addition the interacting spectrum at the same temperature is shown (colored solid).

Dependence on the choice of ω Interval

A form of implicit prior information lies in the choice of the discretization interval $\omega \in [\omega_{\min}, \omega_{\max}]$ along the frequency axis. If we choose it too small, not all relevant frequencies encoded in the data are accessible and the reconstruction fails. In the case of the standard implementation of the MEM, choosing the lower limit of the interval too low adversely affects the reconstruction result, as the limited number of basis functions only contain an oscillatory part close to $\omega_{\min}$ before damping away at higher frequency. This artificial limitation is completely absent in the new Bayesian method.

We find that a too high choice of $\omega_{\min}$ and a too low choice of $\omega_{\max}$ affects the outcome of our reconstruction significantly beyond the statistical error-bars. However it is evident from Fig. 28 and Fig. 29 that by allowing the reconstruction to proceed on an increasingly larger interval one finds that the peak position stabilizes while the peak width is still weakly affected due to the change in prior normalization occurring between different choices of the frequency interval length.

Systematics of the MEM

In order to compare our study's results to previous work based on the MEM, we have carried out the reconstruction of spectral information based on the popular implementation by Bryan. In this approach the search space from which the spectra are chosen is restricted to have dimension equal to the number of data points. Furthermore the basis functions of this search space are constructed from a singular value decomposition of the convolution kernel.

Again we use $N_\omega = 1200$ and a numerical value of $\tau_{\max}^{\mathrm{Num}} = 20.$ but here the frequency interval is taken to span $[-0.15, 25]$ in order for the oscillatory part of the restricted search space basis functions to extend into the positive frequency domain. Our minimizer is set to accept an extremum of the $Q = L - \alpha S$ functional if the step size becomes less than 5×10^{-9}. The standard alpha

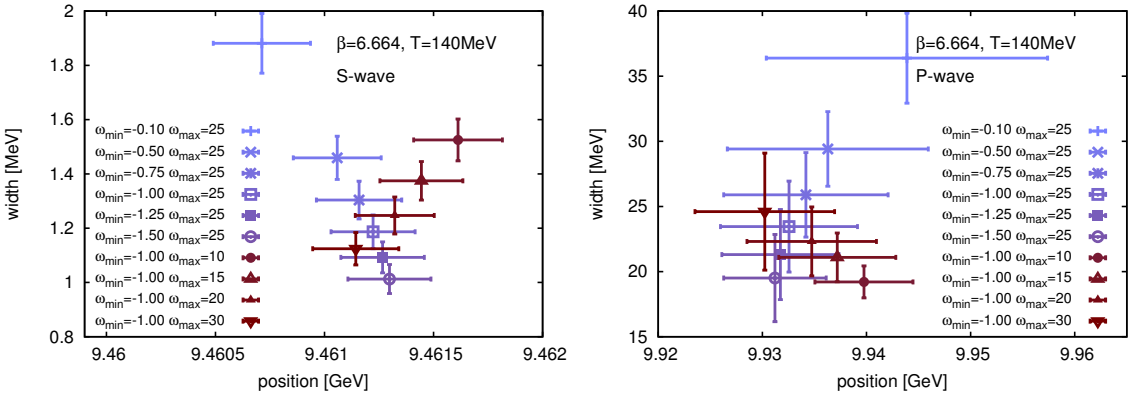

FIG. 28. At 140MeV: Dependence of the reconstructed peak position and peak width on different choices of the frequency interval for the Υ (left) and χ_{b1} (right) channel. While a too narrow choice of $[\omega_{\min}, \omega_{\max}]$ leads to significant changes in the reconstructed values, peak positions stabilize to a plateau at large enough interval lengths. The Peak width is slightly less stable, since it depends more strongly on the default model normalization, which changes with each different choice of $[\omega_{\min}, \omega_{\max}]$.

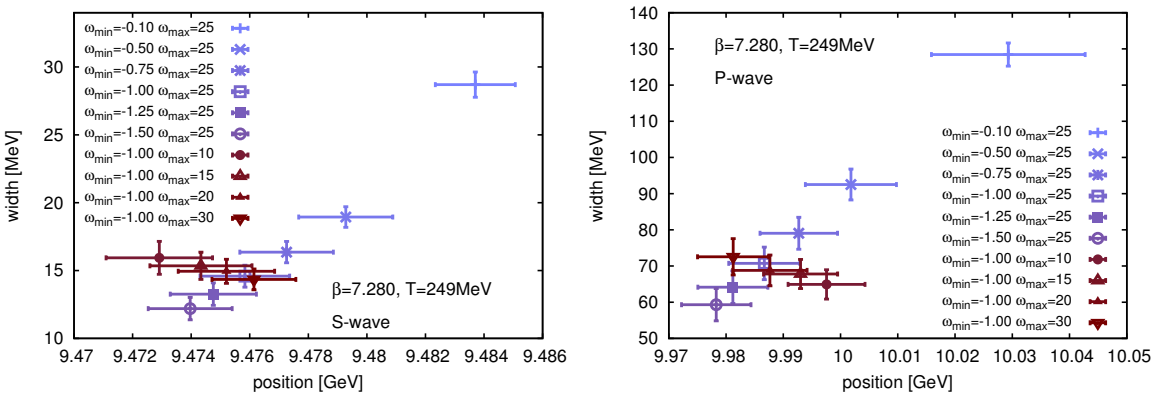

FIG. 29. At 248MeV: Dependence of the reconstructed peak position and peak width on different choices of the frequency interval for the Υ (left) and χ_{b1} (right) channel. While a too narrow choice of $[\omega_{\min}, \omega_{\max}]$ leads to significant changes in the reconstructed values, peak positions stabilize to a plateau at large enough interval lengths. The Peak width is slightly less stable, since they depend more strongly on the default model normalization, which changes with each different choice of $[\omega_{\min}, \omega_{\max}]$.

integration is carried out for each Jackknife bin to arrive at the spectral functions shown in Fig. 6 and Fig. 11.

One finds that the reconstruction is not only less stable but also shows rather washed out spectral features. The ground state peak is not a Lorentzian but instead appears more Gaussian with its width roughly an order of magnitude larger compared to the new Bayesian reconstruction method. It is difficult to compare the obtained peak positions and widths as their values depend crucially on the choice of the frequency interval.

As shown in Fig. 30 and Fig. 31 the reconstructed position can be shifted to significantly lower and the width to significantly higher values if the frequency interval is extended further into the negative regime. Essentially it is possible to melt bottomonium with the MEM from a choice of frequency interval alone, which is in stark contrast to the behavior of the new method which clearly shows a plateau of the reconstructed values for large enough intervals.

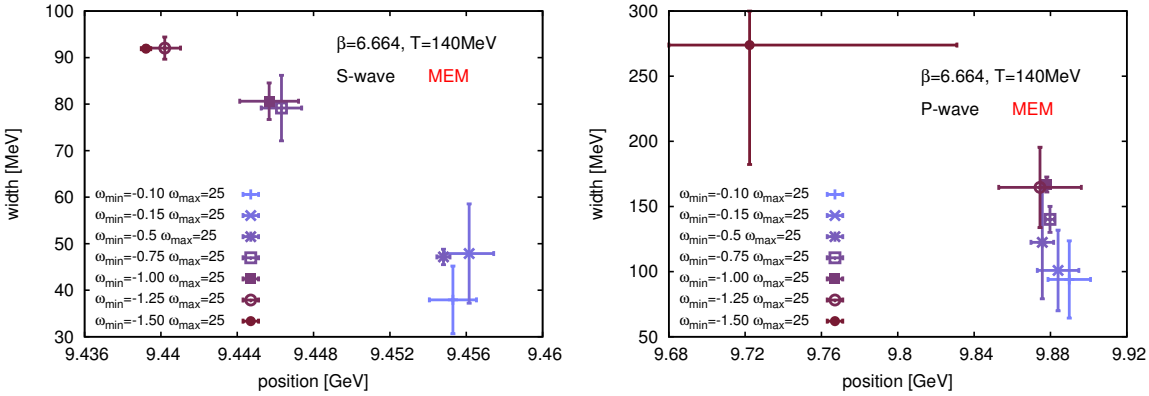

FIG. 30. At 140MeV: The dependence of the Maximum Entropy reconstructed peak width and position on different choices for the frequency interval in the Υ (left) and χ_{b1} (right) channel. We find as expected from the arguments laid out in subsection on the choice of the ω interval that moving $\omega_{\min}$ to lower and lower values degrades the quality of the reconstruction. Both the peak position moves to smaller values while the width grows. Neither in the Υ nor in the χ_{b1} a plateau is reached within the inspected choices. Note that the error bars beyond $\omega_{\min} \leq -1$ cannot be trusted as the minimizer remains at values of $L > 100$. This is a clear indication for a lack of oscillatory degrees of freedom in the search space basis functions.

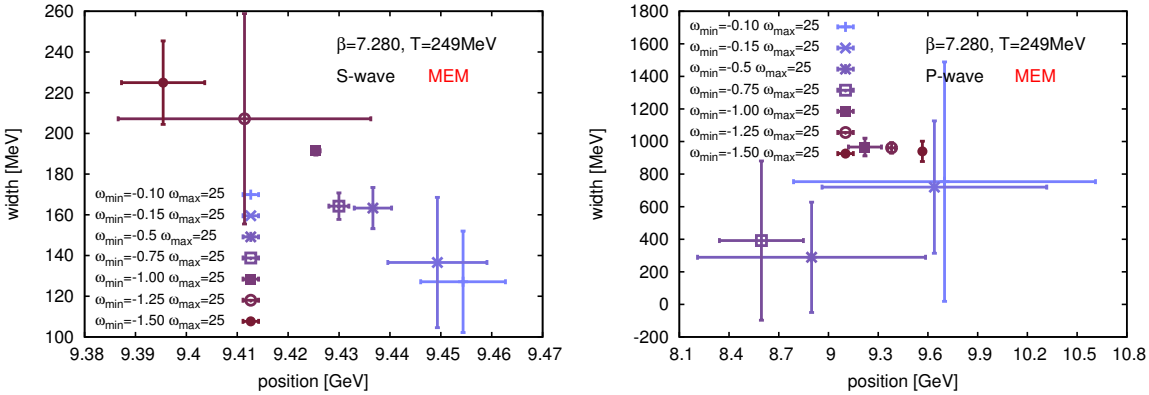

FIG. 31. At 249MeV: The dependence of the Maximum Entropy reconstructed peak width and position on different choices for the frequency interval in the Υ (left) and χ_{b1} (right) channel.

Appendix B: Tests of the NRQCD discretization

The applicability of an effective field theoretical description relies on the presence of a separation of scales. In the case of heavy quark pairs in continuum NRQCD, it is characterized by $\Lambda_{\rm QCD}/M_b \ll 1$, $T/M_b \ll 1$ and $\mathbf{p}^2/2M_b \ll 1$. On the lattice the latter translates into a ratio between the discretized lattice momenta

$$\hat{\mathbf{p}}^2 = 4\sum_{i=1}^{3} \sin^2\Big(\frac{\pi n_i}{N_s}\Big), \quad n_i = -\frac{N_s}{2}+1,\ldots,\frac{N_s}{2} \qquad \text{(B1)}$$

of the first Brillouin zone and the effective mass parameter $\hat{M} = 2n\xi a_s M_b$, where ξ denotes the physical lattice anisotropy and n characterizes the choice of Euclidean time discretization in the NRQCD propagator equation of motion (3).

Analyzing non-interacting lattice NRQCD Ref. [44] showed that for isotropic lattices ($\xi = 1$) the choice $n = 1$ is sufficient to obtain a stable high momentum behavior, as long as $a_s M_b > 3$, respectively $a_s M_b > 1.5$ for $n = 2$. Otherwise the expansion in powers of the velocity (respectively inverse rest mass) breaks down and the high frequency regime of the theory becomes ill-defined. This is a direct consequence of the EFT not possessing a naive continuum limit. This constraint on n related to the validity of the NRQCD expansion is reflected also in the free dispersion relation

$$\begin{aligned} a_\tau E_{\hat{\mathbf{p}}} &= 2n\mathrm{Log}\Big[1 - \frac{1}{2}\frac{\hat{\mathbf{p}}^2}{2n\xi a_s M_b}\Big] \\ &+\mathrm{Log}\Big[1 + \frac{(\hat{\mathbf{p}}^2)^2}{16n\xi(a_s M_b)^2} + \frac{(\hat{\mathbf{p}}^2)^2}{8\xi(a_s M_b)^3} - \frac{\hat{\mathbf{p}}^4}{24\xi(a_s M_b)}\Big] \end{aligned} \qquad \text{(B2)}$$

that follows from Eq. (3). Here the requirement of a positive argument in the logarithm leads to e.g. $a_s M_b > 1.5$ for $n = 2$. From Eq. (B2) the free spectra are computed

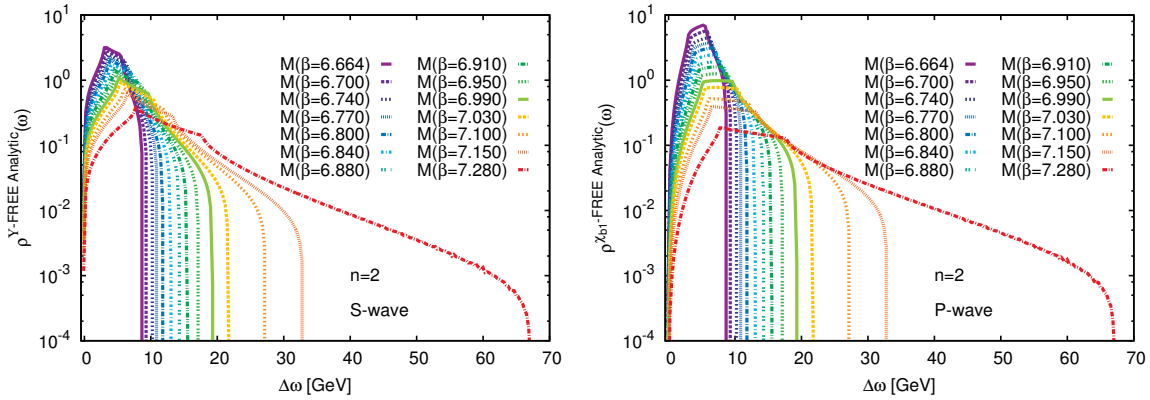

FIG. 32. The analytic free S-wave (left) and P-wave (right) spectral functions according to Eq. (B3) for $n = 2$ with the effective mass parameter chosen to agree with the values of the fully interacting lattices ($N_s = 384$ used to obtain smooth curves). While lattice artifacts dominate the region above 8GeV (i.e. above the first kink), the physics of the bound state resides at frequencies below 1GeV.

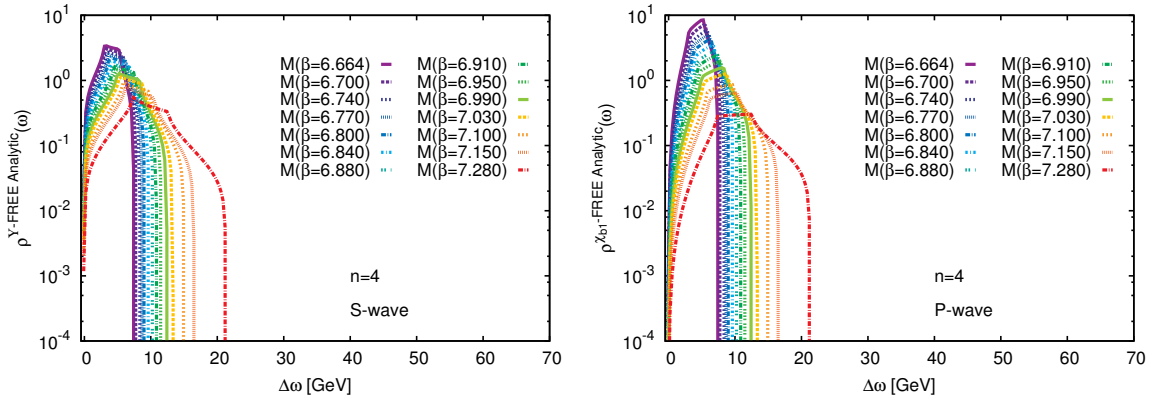

FIG. 33. The analytic free S-wave (left) and P-wave (right) spectral functions according to Eq. (B3) for $n = 4$ with the effective mass parameter chosen to agree with the values of the fully interacting lattices ($N_s = 384$ used to obtain smooth curves). Note that in comparison to Fig. 32 the high frequency range is much more limited, while the amplitude of the kink structure is increased. We also see that the region of relevant frequencies $w < 1$GeV does not change appreciably.

via

$$\rho_S(\omega) = \frac{4\pi N_c}{N_s^3} \sum_{\hat{\mathbf{p}}} \delta(\omega - 2E_{\hat{\mathbf{p}}}),$$
$$\rho_P(\omega) = \frac{4\pi N_c}{N_s^3} \sum_{\hat{\mathbf{p}}} \hat{\mathbf{p}}^2 \delta(\omega - 2E_{\hat{\mathbf{p}}}), \qquad \text{(B3)}$$

as laid out e.g. in the appendix of [25, 26]. We note that a difference in the overall normalization between the analytic and lattice regularized free spectra exists. I.e. if we were to calculate from Eq.(B3) the corresponding Euclidean correlator its value at $\tau = 0$ is larger than $D(0)$ obtained from Eq.(3) with unit links. One reason is that the full dispersion relation that enters Eq.(B3) is only applied to the lattice propagator from time step $\tau/a > 1$.

Since on the highest temperature lattices deployed in our study the product $a_s(\beta = 7.280)M_b = 1.559$ lies only slightly above the limiting value derived from non-interacting lattice NRQCD, we need to ascertain, whether the results from our choice of $n = 2$ are good enough to capture the bound state physics we are interested in. This question is related to the fact that all reconstructed spectra shown in this manuscript do contain finite contributions beyond the inverse lattice spacing, where in a relativistic description, one would expect a relatively sharp cutoff. For NRQCD this is indeed not the case and EFT induced artifacts can populate frequencies up to much larger (but finite) values, as shown in the analytically determined free NRQCD lattice spectral functions given in Fig. 32. Note that in case of a breakdown of the NRQCD approximation, the spectrum would be essentially unbounded in ω.

To check whether changes in the high frequency regime of the theory affect the reconstruction of the ground state peak investigated in this study, we either need to generate configurations with different physical anisotropy or change the NRQCD temporal discretization parameter to larger values than our standard setting $n = 2$. We choose the latter option and present the tests, compar-

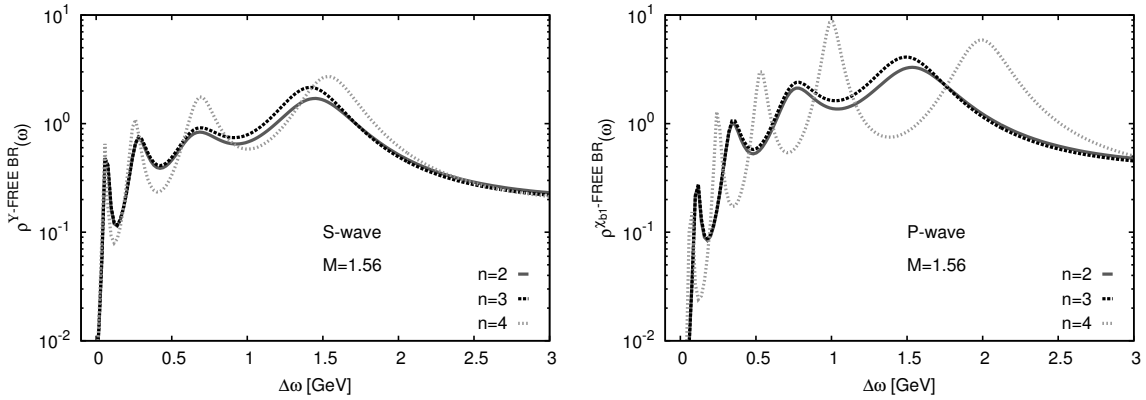

FIG. 34. The free spectra for S-wave (left) and P-wave (right) extracted from the free NRQCD correlators, based on the effective mass parameters $a_s(\beta = 7.280)M_b = 1.56$ and three different values of the parameter $n = 2, 3, 4$. Consistent with expectations, the spectra are increasing in amplitude at higher frequencies $\omega > 1$GeV. In the S-wave channel the number of reconstructed wiggles remains stable, while there seems to be a slight increase in the amplitude of the ground state peak at $n = 4$. In the P-wave channel for $n = 4$, we obtain an additional wiggle but do not find indications that the strength of the low frequency structures changes.

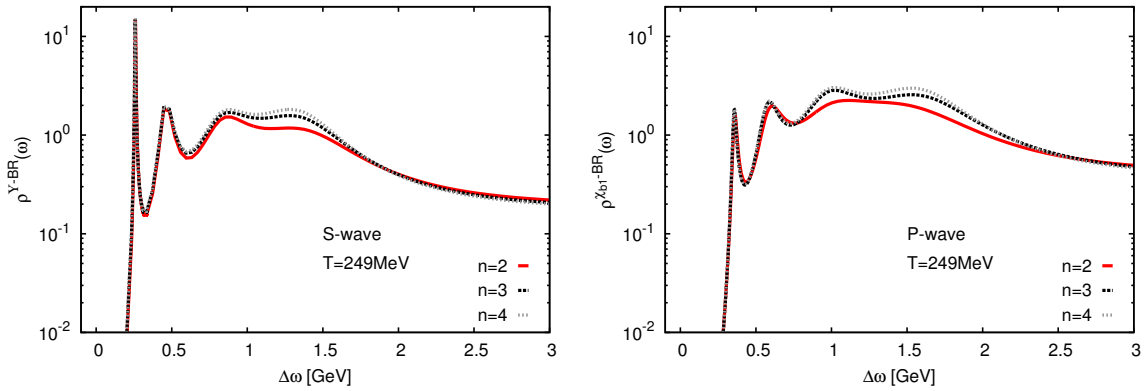

FIG. 35. The interacting spectra for S-wave (left) and P-wave (right) extracted from the NRQCD correlators measured on the $T > 0$, $\beta = 7.280$ lattices at three different values of the parameter $n = 2, 3, 4$. Again consistent with expectations the spectra are increasing in amplitude at higher frequencies $\omega > 1$GeV. In both channels the ground state peak is virtually unaffected by the changes in the high frequency behavior of NRQCD.

ing $n = 2, 3, 4$ in the following.

To understand the change induced by increasing n to four, we inspect the corresponding analytic free spectra plotted in Fig. 33. The most obvious effect is a significant reduction of the maximum frequency, up to which the lattice EFT artifacts populate the spectrum. We find it to move towards the origin by more than a factor of three. Interestingly at the same time the amplitude of the kinked structure is slightly larger than at $n = 2$. The most important fact however is that the region of low frequencies $\omega < 1$GeV in which the bound state physics is located does not change appreciably with changing the NRQCD effective temporal step size.

With this intuition at hand, we proceed to measure the lattice NRQCD bottomonium correlation functions both on non- and fully interacting lattices, using the different settings $n = 2, 3, 4$ and subsequently perform spectral reconstructions. We restrict ourselves to $\beta = 7.280$, since here the mass parameter $a_s M_b = 1.56$ is closest to the free NRQCD limit and the non-interacting spectra show the most pronounced changes. Of interest is in particular, whether the change in discretization affects the conclusion drawn about the presence of a well defined ground state peak in the P-wave channel at $T = 249$MeV.

The free spectral functions are shown in Fig. 34. We find that, as hinted at by the analytically calculated free spectra, the amplitude of $\rho(\omega)$ goes up as we increase n at frequencies above 1GeV. In the S-wave channel the number of reconstructed wiggles remains the same between all choices of n and the lowest lying peak only shows a minute increase in strength for $n = 4$, much smaller than the factor ten separating it from the interacting spectrum as seen in Fig. 9. In the P-wave channel for $n = 4$ the reconstruction shows an additional wiggle, however there are no indications that the overall strength at small frequencies increases. In all, these findings indicate that the

free spectral functions obtained numerically with $n = 2$ at the relevant (unshifted) frequencies $\Delta\omega < 1$GeV are robust against changes in the high frequency behavior of NRQCD.

As final step we need to perform the same comparison with the spectra based on NRQCD correlators from the fully interacting lattices, evaluated with $n = 2, 3, 4$. The results are shown in Fig. 35. Just as we saw in the case of the free spectral functions, stepping up the value of n increases the amplitude of the spectrum at frequencies above 1GeV. As is clearly visible, both in the S-wave (left) and P-wave (right) channel, the lowest lying peak structure remains virtually unchanged as we vary n. This is a strong indicator that the spectra obtained at $n = 2$ are robust against changes in the high frequency behavior of NRQCD and thus are a reliable representation of the underlying QCD bound state physics. Together with the observed robustness of the free spectral function reconstruction, these findings reassure us that the observation of a well defined peak structure in the P-wave channel at $T = 249$MeV is not simply an artifact, neither of the Bayesian reconstruction nor of the discretization prescription of the deployed EFT.

[1] N. Brambilla, S. Eidelman, B. K. Heltsley, R. Vogt, G. T. Bodwin, E. Eichten, A. D. Frawley and A. B. Meyer *et al.*, "Heavy quarkonium: progress, puzzles, and opportunities," Eur. Phys. J. C **71** (2011) 1534 [arXiv:1010.5827 [hep-ph]].

[2] N. Brambilla, A. Pineda, J. Soto and A. Vairo, "Effective field theories for heavy quarkonium," Rev. Mod. Phys. **77** 1423 (2005) [hep-ph/0410047].

[3] G. T. Bodwin, E. Braaten and G. P. Lepage, "Rigorous QCD analysis of inclusive annihilation and production of heavy quarkonium," Phys. Rev. D **51** (1995) 1125 [Erratum-ibid. D **55** (1997) 5853] [hep-ph/9407339].

[4] T. Matsui and H. Satz, "J/psi Suppression by Quark-Gluon Plasma Formation," Phys. Lett. B **178** (1986) 416.

[5] F. Karsch, M. T. Mehr and H. Satz, "Color Screening and Deconfinement for Bound States of Heavy Quarks," Z. Phys. C **37** (1988) 617.

[6] H. Satz, "Quarkonium Binding and Dissociation: The Spectral Analysis of the QGP," Nucl. Phys. A **783** (2007) 249 [arXiv:hep-ph/0609197].

[7] C. Baglin *et al.* [NA38 Collaboration], "The Production of J/ψ in 200-GeV/nucleon Oxygen Uranium Interactions," Phys. Lett. B **220** (1989) 471.

[8] R. Vogt, S. J. Brodsky and P. Hoyer, "Systematics of J / psi production in nuclear collisions," Nucl. Phys. B **360** (1991) 67.

[9] R. Rapp, D. Blaschke and P. Crochet, "Charmonium and bottomonium production in heavy-ion collisions," Prog. Part. Nucl. Phys. **65** (2010) 209 [arXiv:0807.2470 [hep-ph]].

[10] S. Chatrchyan *et al.* [CMS Collaboration], "Indications of suppression of excited Υ states in PbPb collisions at $\sqrt{S_{NN}} = 2.76$ TeV," Phys. Rev. Lett. **107** (2011) 052302. [arXiv:1105.4894 [nucl-ex]].

[11] S. Chatrchyan *et al.* [CMS Collaboration], "Observation of sequential Upsilon suppression in PbPb collisions," Phys.Rev.Lett. **109** (2012) 222301 [arXiv:1208.2826].

[12] B. A. Thacker and G. P. Lepage, "Heavy quark bound states in lattice QCD," Phys. Rev. D **43** (1991) 196.

[13] G. P. Lepage, L. Magnea, C. Nakhleh, U. Magnea and K. Hornbostel, "Improved nonrelativistic QCD for heavy quark physics," Phys. Rev. D **46** (1992) 4052 [hep-lat/9205007].

[14] J. Fingberg, "Heavy quarkonia at high temperature," Phys. Lett. B **424** (1998) 343 [hep-lat/9707012].

[15] M. Gyulassy and L. McLerran, "New forms of QCD matter discovered at RHIC," Nucl. Phys. A **750** (2005) 30 [nucl-th/0405013].

[16] B. Muller, "From Quark-Gluon Plasma to the Perfect Liquid," Acta Phys. Polon. B **38** (2007) 3705 [arXiv:0710.3366 [nucl-th]].

[17] M. Laine, O. Philipsen, P. Romatschke and M. Tassler, "Real-time static potential in hot QCD," JHEP **0703** (2007) 054 [arXiv:hep-ph/0611300].

[18] A. Beraudo, J. P. Blaizot and C. Ratti, "Real and imaginary-time $Q\bar{Q}$ correlators in a thermal medium," Nucl. Phys. A **806** (2008) 312 [arXiv:0712.4394 [nucl-th]].

[19] N. Brambilla, J. Ghiglieri, A. Vairo and P. Petreczky, "Static quark-antiquark pairs at finite temperature," Phys. Rev. D **78** (2008) 014017 [arXiv:0804.0993 [hep-ph]].

[20] A. Rothkopf, T. Hatsuda, S. Sasaki, "Proper heavy-quark potential from a spectral decomposition of the thermal Wilson loop," PoS **LAT2009** (2009) 162 [arXiv:0910.2321 [hep-lat]].

[21] A. Rothkopf, T. Hatsuda, S. Sasaki, "Complex Heavy-Quark Potential at Finite Temperature from Lattice QCD," arXiv:1108.1579 [hep-lat].

[22] J. Skilling, S.F. Gull, Lecture Notes-Monograph Series 20 (1991) 341; M. Jarrell and J.E. Gubernatis, Bayesian inference and the analytic continuation of imaginary-time quantum Monte Carlo data, Physics Reports, **269** (1996) 133

[23] M. Asakawa, T. Hatsuda, Y. Nakahara, "Maximum entropy analysis of the spectral functions in lattice QCD," Prog. Part. Nucl. Phys. **46** (2001) 459 [hep-lat/0011040].

[24] G. Aarts, S. Kim, M. P. Lombardo, M. B. Oktay, S. M. Ryan, D. K. Sinclair, J. -I. Skullerud, "Bottomonium above deconfinement in lattice nonrelativistic QCD," Phys. Rev. Lett. **106** (2011) 061602 [arXiv:1010.3725 [hep-lat]].

[25] G. Aarts, C. Allton, S. Kim, M. P. Lombardo, M. B. Oktay, S. M. Ryan, D. K. Sinclair and J. I. Skullerud, "What happens to the Υ and η_b in the quark-gluon plasma? Bottomonium spectral functions from lattice QCD," JHEP **1111** (2011) 103 [arXiv:1109.4496 [hep-lat]].

[26] G. Aarts, C. Allton, T. Harris, S. Kim, M. P. Lombardo, S. M. Ryan and J. I. Skullerud, "The bottomonium spectrum at finite temperature from $N_f = 2 + 1$ lattice QCD," JHEP **1407** (2014) 097 [arXiv:1402.6210 [hep-lat]].

[27] G. Aarts, C. Allton, S. Kim, M. Lombardo, S. Ryan *et al.*,

"Melting of P wave bottomonium states in the quark-gluon plasma from lattice NRQCD," JHEP **1312** (2013) 064 [arXiv:1310.5467].

[28] A. Bazavov, T. Bhattacharya, M. Cheng, C. DeTar, H. T. Ding, S. Gottlieb, R. Gupta and P. Hegde *et al.*, "The chiral and deconfinement aspects of the QCD transition," Phys. Rev. D **85** (2012) 054503 [arXiv:1111.1710 [hep-lat]].

[29] S. Kim, P. Petreczky and A. Rothkopf, "Lattice NRQCD study of in-medium bottomonium states using $N_f = 2+1, 48^3 \times 12$ HotQCD configurations," arXiv:1310.6461 [hep-lat].

[30] Y. Burnier and A. Rothkopf, "Bayesian Approach to Spectral Function Reconstruction for Euclidean Quantum Field Theories," Phys. Rev. Lett. **111** (2013) 182003 [arXiv:1307.6106 [hep-lat]].

[31] Y. Burnier and A. Rothkopf, "A new Bayesian approach to the reconstruction of spectral functions," arXiv:1310.0645 [hep-lat].

[32] J. Beringer *et al.* [Particle Data Group Collaboration], "Review of Particle Physics (RPP)," Phys. Rev. D **86** (2012) 010001.

[33] E. J. Eichten and C. Quigg, "Quarkonium wave functions at the origin," Phys. Rev. D **52** (1995) 1726 [hep-ph/9503356].

[34] A. Jakovac, P. Petreczky, K. Petrov and A. Velytsky, "Quarkonium correlators and spectral functions at zero and finite temperature," Phys. Rev. D **75** (2007) 014506 [hep-lat/0611017].

[35] A. Gray, I. Allison, C. T. H. Davies, E. Dalgic, G. P. Lepage, J. Shigemitsu and M. Wingate, "The Upsilon spectrum and m(b) from full lattice QCD," Phys. Rev. D **72** (2005) 094507 [hep-lat/0507013].

[36] C. T. H. Davies, K. Hornbostel, A. Langnau, G. P. Lepage, A. Lidsey, J. Shigemitsu and J. H. Sloan, "Precision Upsilon spectroscopy from nonrelativistic lattice QCD," Phys. Rev. D **50** (1994) 6963 [hep-lat/9406017].

[37] G. P. Lepage and P. B. Mackenzie, "On the viability of lattice perturbation theory," Phys. Rev. D **48** (1993) 2250 [arXiv:hep-lat/9209022].

[38] T. Umeda, "A constant contribution in meson correlators at finite temperature," Phys. Rev. D **75** (2007) 094502 [arXiv:hep-lat/0701005].

[39] G. Aarts and J. M. Martínez Resco, "Transport coefficients, spectral functions and the lattice," JHEP **0204** (2002) 053 [arXiv:hep-ph/0203177].

[40] P. Petreczky, "On temperature dependence of quarkonium correlators," Eur. Phys. J. C **62** (2009) 85 [arXiv:0810.0258 [hep-lat]].

[41] F. Karsch, E. Laermann, P. Petreczky, S. Stickan, "Infinite temperature limit of meson spectral functions calculated on the lattice," Phys. Rev. **D68** (2003) 014504 [hep-lat/0303017].

[42] G. Aarts, J. M. Martínez Resco, "Continuum and lattice meson spectral functions at nonzero momentum and high temperature," Nucl. Phys. **B726** (2005) 93 [hep-lat/0507004].

[43] N. Brambilla, M. A. Escobedo, J. Ghiglieri, J. Soto and A. Vairo, "Heavy Quarkonium in a weakly-coupled quark-gluon plasma below the melting temperature," JHEP **1009** (2010) 038 [arXiv:1007.4156 [hep-ph]].

[44] C. T. H. Davies and B. A. Thacker, "Heavy quark renormalization parameters in nonrelativistic QCD," Phys. Rev. D **45** 915 (1992).